UNIVERSITY OF HELSINKI

https://helda.helsinki.fi

Highly dispersed atomic layer deposited CrOx on SiO2 catalyst with enhanced yield of propylene for CO2 –mediated oxidative dehydrogenation of propane

Daresibi, Fatemeh Gashoul; Khodadadi, Abbas Ali; Mortazavi, Yadollah; Huotari, Simo; Ritala, Mikko

2022-06

Elsevier Scientific Publ. Co

http://hdl.handle.net/10138/576398

Daresibi, F G, Khodadadi, A A, Mortazavi, Y, Huotari, S & Ritala, M 2022, 'Highly dispersed atomic layer deposited CrOx on SiO2 catalyst with enhanced yield of propylene for CO2 –mediated oxidative dehydrogenation of propane', Molecular catalysis, vol. 526, 112396. https://doi.org/10.1016/j.mcat.2022.112396

Downloaded from Helda, University of Helsinki institutional repository. https://helda.helsinki.fi

This is an electronic reprint of the original article.

This reprint may differ from the original in pagination and typographic detail.

Please cite the original version.

Highly dispersed atomic layer deposited CrO_x on SiO_2 catalyst with enhanced yield of propylene for CO_2 –mediated oxidative dehydrogenation of propane

Fatemeh Gashoul Daresibi [a], Prof. Abbas Ali Khodadadi *[a], Prof. Yadollah Mortazavi [a], Prof. Simo Huotari [b], Prof. Mikko Ritala [c]

[a] Department of Chemical Engineering
University of Tehran
Address: Catalysis and Nanostructured Materials Research Laboratory, School of Chemical Engineering, University of Tehran, P.O. Box: 11155/4563, Tehran, Iran,
E-mails: fatemeh.gashoul@ut.ac.ir, * khodadad@ut.ac.ir (Corresponding author) phone number: +98 2161112212 , mortazav@ut.ac.ir

[b] Department of Physics
University of Helsinki
Address: P.O. Box 64, 00014, Helsinki, Finland
E-mail: simo.huotari@helsinki.fi

[c] Department of Chemistry
University of Helsinki
P.O. Box 64, 00014, Helsinki, Finland
E-mail: mikko.ritala@helsinki.fi

Supporting information for this article is given via a link at the end of the document.

Abstract:

The increasing worldwide demand for propylene and the necessity of CO_2 mitigation attracted the attention of scientists to focus on CO_2-oxidative dehydrogenation of propane (CO_2-ODHP). In this regard, CrO_x/SiO_2 catalyst is an important and conventional option. Herein, we studied the atomic layer deposition (ALD) of CrO_x on silica to increase the propylene production by increasing the dispersion of the catalyst. For ALD synthesis of CrO_x/SiO_2 catalyst, $Cr(acac)_3$ and synthetic air were used as metal precursor and oxidant. The catalysts were examined in the CO_2-ODHP reaction and their characteristics were compared to their impregnation counterparts using UV-Vis DRS, Raman, XANES, HRTEM and STEM-EDS mapping, H_2-TPR, NH_3-TPD and TPO. The ALD catalysts have shown up to 2 times higher acidity and enhanced reducibility compared to the impregnation catalysts. The presence of mainly Cr(VI) with a pre-edge peak at 5.994 keV in both series of catalysts was confirmed by XANES. UV-Vis DRS and Raman spectroscopy revealed the higher contents of active polymeric Cr(VI) species in the ALD ones. The dark field HRTEM and STEM-EDS mapping represented higher dispersion of chromium oxide particles in ALD catalysts. In CO_2-ODHP, the ALD catalysts showed up to 18 and 15% promotion in propane conversion and propylene yield.

Keywords:

Atomic layer Deposition, Polymeric Chromium Oxide, Dispersion, CO_2, Propane

1. Introduction

Oxidative dehydrogenation of propane using the greenhouse gas of CO_2 (CO_2-ODHP) with a tandem target of reducing CO_2 emissions and increasing the marketable propylene production, as a key feedstock of several petrochemical industries, has recently attracted the attention of heterogenous catalysis researchers [1,2]. The reaction proceeds either through oxidative pathway over redox-type transition metal oxides (for example chromium and vanadium oxides), or non-oxidative mechanism over non-redox main group metal oxides (for example gallium oxide) via direct dehydrogenation of propane (DHP) followed by reverse water-gas shift (RWGS). However, one cannot define an unambiguous boundary between the two pathways. In other words, each of these mechanisms can, to some extent, occur over both series of catalysts. CO_2 as a mild oxidant, on the one hand, heals the produced oxygen vacancies while decreases the over-oxidation of propane and propylene to CO_x that is highly detrimental in exothermic conditions of the common O_2-ODHP reaction. On the other hand, this CO_2 promotes the direct dehydrogenation by shifting the equilibrium to the propylene side with consuming H_2 in RWGS reaction and removing the produced coke through reverse Boudouard reaction [2–4]. As CO_2 is a thermodynamically stable molecule, a high performance catalyst is required to fulfill both CO_2 mitigation and propylene production purposes in each of the reported pathways. A variety of catalysts were reported for the CO_2-ODHP reaction with various range for selectivity and conversion at different time on streams (TOS). Among them, chromium oxides dispersed typically over the mesoporous silica based supports, can be pointed as the most important active sites for CO_2-ODHP reaction [4–7]. Chromium oxide based active sites are also suggested to take part in both redox and non-redox mechanisms. It has been proposed that at the begining of the reaction the main state of chromium oxide belongs to Cr (VI) which plays either the role of the precusor for Cr(III) and Cr(II) species under the reaction conditions or the main active site to generate the Cr(VI, III) redox cycle [4,8].

In order to enhance the activity of the supported CrO_x catalysts in the propane dehydrogenation reaction, research studies have shown the necessity of providing high dispersion of Cr species [8–13]. The higher dispersion of CrO_x species increases the number of medium acid sites and consequently promotes the catalytic activity [13].

In attempting to investigate the inherent nature of chromium oxide sites, research studies show that CrO_x have several types including mostly the isolated Cr(VI), polymeric Cr(VI) and crystalline Cr(III) forms [8,14–16]. Currently, it is not clearly known that which type of Cr(VI) species are active sites in CO_2-ODH. Some researchers have focused on increasing the number of isolated Cr(VI) species to change their behavior in CO_2-ODHP reaction. Cheng et al.[17] reported the utilization of silicalite as support material instead of common high surface area SBA-15 to reach single site Cr(VI) which resulted in higher activity and longevity of the catalyst in CO_2-ODH of ethane which might behave similarly in CO_2-ODHP. Aiming the higher performance of chromium oxide in dehydrogenation of propane, Zhang et al. [8] have used the flowing air calcination method rather than traditional calcination in O_2 deficit furnaces to increase the population of surface isolated Cr(VI) active sites and prevent the polymerization of them.

In contrast, Baek et al. [9], have reported the less activity of isolated chromium oxides in CO_2-ODHP due to its decreased affinity toward reduction and participation in the reaction cycle while polymerized Cr(VI) species have shown greater performance due to their higher reducibility. By focusing on propane dehydrogenation only, Dedong He [15] reported the less activity and selectivity of isolated Cr(VI) due to their lower reducibility. Their results show improved values of activity and selectivity for non-isolated Cr(VI) species. Wang et al. [14], used silicalite-1 support with the unique silanol nests which results in high dispersion to impregnate the chromium nitrate salt on it and form chromium oxide catalysts with both isolated and polymeric Cr(VI) species. They found more activity and less selectivity of polymeric Cr(VI) oxides than the isolated Cr(VI) oxides, and the stronger trends with the increase of the polymerization degree.

Zhang et al. [16] reported the higher performance of Ce-promoted CrO_x catalyst in propane dehydrogenation, due to the decreased number of inactive isolated Cr(VI).

Considering the above arguments on the type of Cr(VI)O species, one can find the strong emphasis on the dispersion of the chromium oxides, the degree of polymerization and prevention of the formation of less active CrO_x crystals. The first choice in this regard, is to change the catalyst preparation method. This way, an easy, fast, inexpensive and common method for the synthesis of most catalysts including supported CrO_x is incipient wetness impregnation. However, this method does not give a catalyst with enough control on size distribution and results in the serious aggregation of the active species and subsequently the formation of crystalline forms [8]. In this regard, we decided to concentrate on atomic layer deposition (ALD) method as one of the attractive alternative methods other than wet ones that recently has shown great results in catalysis. In the flat film applications, like semi-conductors, ALD is a well-established sequential method capable of depositing uniform and conformal surface layers with angstrom level thicknesses [18,19]. This method was, in the same way, found a highly efficient method for the production of supported catalysts with extremely high control on uniformity, composition, structure and support-active phase interactions [20–25]. In the case of dehydrogenation reactions, ALD method was utilized for either deposition of the active site alone [23,26,27] or over-coating of the target site with layers of an effective metal oxide to increase the selectivity, activity or longevity of the catalyst [28–30]. For deposition of the active sites alone, Yang and colleagues in a recent research [23] showed the formation of isolated vanadium oxides over aluminium oxide in the first cycle of ALD in a commercial vacuum reactor while the poly-vanadate species were formed in the next cycles keeping the dose time of precursor at a fixed short period of 200 s. Feng et al. [31], have used the ALD method with a precursor dose time of 45 s for the deposition of vanadium oxide and the investigation of the activity of VO_x isolated

monomers and polyvanadates with various degrees of polymerization in oxidative dehydrogenation of cyclohexane.

Herein, we have synthesised the silica supported CrO_x catalysts in a home-built atmospheric pressure ALD reactor and compared them with their impregnation synthesized counterparts in conversion and selectivity for dehydrogenation of propane with CO_2. Our studies illustrated the higher activity of ALD catalysts with almost the same level of selectivity of propylene in CO_2-ODHP reaction. The results of characterizations reveal that the ALD catalysts developed higher extent of active polymeric Cr(VI) species and higher dispersion of CrO_x particles.

2. Experimental

2.1. Catalyst Synthesis by Atomic Layer Deposition (ALD) Method

First, the density of surface –OH groups on silica gel (Sigma-Aldrich, Davisil ™, 150Å, 99+%) was measured by the Grignard reaction. Details of the Grignard procedure and experimental setup is reported in the **S1.** section of Supplementary Information.

Then, the ALD of CrO_x on silica was performed in a home-built vertical reactor comprising of two heating zones (See **Figure S.2**). Chromium(III) 2,4-pentanedionate, $Cr(acac)_3$ (Merck, 99.99%) was used as the chromium precursor and synthetic air (N_2:O_2 of 80:20, Purity: 99.9%) as the oxidant. Ar (Purity: 99.999%) at a flow rate of 110 sccm was used as the carrier gas. The main ALD steps are similar to what was reported by Taheri Najafabadi et al. [20] and include: (1) degassing the silica support placed in the ALD reactor zone in Ar at 200 °C for 1 h prior the reaction, to remove air and weakly adsorbed H_2O, (2) reactive chemisorption of $Cr(acac)_3$, sublimed at 170 °C, on the silica support at various temperatures including 170-270 °C under 110 sccm Ar flow (3) purging the reactor with Ar at 200 °C for 60 min (4) oxidizing the remaining acac ligands of Cr by flowing synthetic air and finally (5) purging with Ar to remove the remaining gas-phase reactants and by-products. During all steps, the effluent gas was passed through a gas

cell in an FTIR spectrometer for analysis of the gaseous products. The schematic illustration of the reactive chemisorption step of ALD reaction is shown in **Figure 1**.



Figure 1. Schematic flow diagram of the first step of reactive chemisorption of $Cr(acac)_3$ on silica in atomic layer deposition process

Different CrO_x loadings on silica were obtained by changing the $Cr(acac)_3$ dose time in the reactive chemisorption step. The samples were denoted based on the CrO_x deposition method and Cr weight percentage measured by ICP, for example ALD-Cr 0.72% for ALD synthesized catalyst sample with 0.72 wt % of Cr on silica.

2.2. Catalyst Synthesis by Impregnation Method

For the synthesis of catalysts with the conventional incipient wetness impregnation method, proper amount of the nitrate precursor, $Cr(NO_3)_3.9H_2O$ (Merck, for analysis EMSURE), was dissolved in distilled water with a volume equal to the pore volume of the silica support. Then, the solution was added in a dropwise manner to the silica powder. The powder was then dried in an oven at 80 °C for 12 h. The calcination was carried out at 600 °C in the flowing synthetic air, as for the ALD catalysts. The impregnated catalysts are denoted as Imp-Cr X% where X represent the Cr loading determined by ICP.

2.3. Catalysts Characterizations

The Cr loading was measured by inductively coupled plasma-optical emission spectroscopy (ICP-OES) method using a VISTA-PRO instrument (Varian Inc.).

Thermogravimetric analysis (TGA), differential thermal analysis (DTA) and differential thermal gravimetric (DTG) analysis of ALD precursor was performed from room temperature to 600 °C with a heating rate of 10 °C.min^{-1} under flowing N_2 using a

Universal TA instrument (SDT Q600 V20.9). Prior to the measurement, the sample was degassed at 120 °C for 2 h followed by cooling down to room temperature.

X-Ray powder diffraction (XRD) patterns were collected on a PANalytical X'pert pro diffractometer with a Co Kα X-ray source. Samples were measured with a step size of 0.02 °.s^{-1} in the 2θ range of 5-80 using 40 kV and 40 mA X-ray source.

High resolution transmission electron microscope (HRTEM), High-angle annular dark-field (HAADF)-STEM imaging and its corresponding energy dispersive spectroscopy (EDS) data were taken on a FEI- G2 Tecnai HRTEM instrument at 200 kV. Samples were prepared by dispersing the dry powder in ethanol and placing a drop of the suspension on a carbon-coated Cu TEM grid. The d-spacing value was calculated using Digital Micrograph package of Gatan Microscopy Suite by firstly applying Fourier transform (FFT), then masking the target spot and finally using the inverse FFT (IFFT).

FTIR of Cr-species on silica was performed on a PerkinElmer Spectrum RX I FT-IR spectrometer. All the samples were diluted with high purity KBr and the resulting mixture was palletized under 15 bar pressure for about 5 min. The analysis was carried out at a resolution of 2 cm^{-1}. The spectra were normalized and deconvoluted to provide more information through comparison of the spectra of different catalysts.

UV-Vis diffuse reflectance spectra (UV-Vis DRS) were measured on a Specord 210 Plus Analytik Jena UV-Vis spectrometer equipped with an integrating barium sulfate sphere, a deuterium arc lamp as the UV light source and a halogen lamp as a visible radiation source. Spectra were collected at room temperature in the range of 200-1100 nm with a resolution of 4 nm and counting rate of 50 nm.s^{-1}.

Raman spectra of samples were collected with a high energy Raman laser of 457 nm on a UniDRON, Confocal microscope Raman/PL spectroscopy system.

NH_3 chemisorption on the catalysts was studied by temperature programmed desorption (TPD) methods in a U-shape quartz reactor on a Quantachrome ChemBET-3000

equipment. The as-synthesized catalyst was activated under flowing synthetic air at 600 °C, flushed with He and then cooled down to 100 °C under flowing He. Then, pure NH_3 was passed through the catalyst bed for 15 min, followed by purging with He for 1 h. Subsequently, NH_3-TPD was performed using 10 sccm of He as carrier gas, while the catalyst sample was heated with a rate of 10 °C.min^{-1} from 100 to 600 °C. The NH_3 desorption products in the effluent gas were detected on a thermal conductivity detector (TCD).

Temperature programmed reduction (TPR) analyses were carried out on a Quantachrome ChemBET-3000 equipped with a thermal conductivity detector (TCD) using 7% H_2 in Ar with a heating rate of 10 °C.min^{-1}. The instrument was calibrated with Ag_2O (Merck, for analysis 99+ EMSURE) for quantitative measurements of H_2 consumption. In all tests, 50 mg of the as-prepared catalyst was activated similar to the NH_3-TPD, purged with N_2 and cooled down to RT under flowing N_2. Then, the TPR analysis was performed over the temperature range of RT to 950 °C.

The X-ray Absorption Near Edge Spectra (XANES) were collected at Cr K-edge (5.98 keV) on a Johann-type Laboratory-Scale XANES Set-ups [32]. **Figure S.3** shows a schematic illustration of the set-up. The X-ray source was a 1.5 kW fine focus X-ray diffraction glass tube with an Ag anode. The monochromator was a spherically bent Si(333) crystal analyser with a bending radius of 0.5 m and surface diameter of 100 mm [33]. Based on the required amount of Cr for the optimum XAS characterization, a mixture of catalyst and starch was made to provide an appropriate robust pellet. Cr_2O_3 and CrO_3 were used as standard compounds to assess the presence of Cr(III) and Cr(VI) in the catalyst samples. The data was recorded in transmission mode and the resulting transmission intensities were used in the Beer-Lambert law to measure the absorption coefficient (Eq. 1) [32].

$$\mu x = -\ln\left(\frac{I - y_{bg}}{I_0 - y_{0,bg}}\right) \quad \text{Eq.1}$$

Where I, I_0 were measured in the presence and absence of the sample, and y_{bg} and $y_{0,bg}$ are the linear fits to their background signals respectively, x is the thickness of the sample, and μ the absorption coefficient that represents the XANES spectrum. A linear pre-edge background was subtracted from the measured XANES spectra and they were normalized to an equal area within the measured energy interval.

Textural parameters including specific surface area, pore size distribution, and pore volume were determined from adsorption-desorption isotherm measured with liquid nitrogen in vacuum on a Belsorp Mini II instrument. Prior to the measurements, all the samples were degassed at 300 °C and in vacuum for 3 h.

2.4. Catalytic Reactivity Measurement

The CO_2-ODHP reaction was carried out at atmospheric pressure using a down-flow fixed-bed quartz micro-reactor, (**Figure S.4**) in the middle of which 400 mg of a catalyst was placed. The reaction temperature was measured with a K-type thermocouple located inside the catalyst bed and controlled by a PID temperature controller. The 30 sccm gas flow, composed of propane, CO_2 and Ar with molar ratios of 1:5:14 respectively, was fed to the reactor. Inlet gas flow rates were controlled using three calibrated mass flow controllers (UNIT instruments LTD). Blank tests for bare silica were conducted under similar reaction conditions.

The reactants and products were analysed with an on-line Varian CP 3800 gas chromatograph equipped with two capillary columns in series for separation of hydrocarbons (CP-Sil 5CB 1.5, 30 m length, 0.530 mm I.D. and Al_2O_3/KCl, 50 m length, 0.530 mm I.D. respectively) in parallel with two different packed columns for separation of CO_2 (HayeSep C 6 ft * 1/8 in., mesh 80/100) and CO (Molecular Sieve 13X 3 ft * 1/8 in., mesh 80/100). The gas chromatograph consisted of two 0.250 ml sample loops, a

10-way valve and two 6-way valves supported by VICI Valco actuators. FID at 210 °C and methanizer at 410 °C were used for proper detection of hydrocarbons and carbon oxides (CO and CO_2). **Figure S.5** shows one of many chromatograms of the reaction products and **Table S1-S4** provides the information of GC gas pressure and flow rate, valve switching, and oven temperature program.

Propane conversion (X), was calculated using Eq.2 [8]:

$$X=100\times\left(\frac{propane_{in}-propane_{out}}{propane_{in}}\right) \quad \text{Eq. 2}$$

Propylene selectivity (S) was calculated as follow (Eq.3) [8]. It is worth noting that, in addition to the methane, ethylene and trace amounts of ethane there was not any other detectable hydrocarbons in any experiments. In addition, the carbon balance was ranging from 95-100%.

$$S=100\times\left(\frac{n_{propylene}}{n_{propylene}+\frac{2}{3}n_{ethylene}+\frac{2}{3}n_{ethane}+\frac{1}{3}n_{methane}}\right) \quad \text{Eq. 3}$$

Then, in accordance with literatures [5,13,34] the reaction rates were normalized by dividing moles of propane converted per second to the total moles of Cr loading of each catalyst, and reported as specific reaction rate (s^{-1}).

2.5. Deactivation of catalysts

For the study of deactivation causes, we first measured the relative deactivation rate (%) from the catalyst performance TOS data by using Eq. 4:

$$\text{Relative Deactivation Rate} = 100\times\left(\frac{X_5-X_{100}}{X_5}\right) \quad \text{Eq. 4}$$

where X_5 and X_{100} are the propane conversion at TOS of 5 and 100 min respectively.

Then, we exposed the catalysts to the reaction feed with a TOS of 6 h, followed by cooling to room temperature under flowing Ar. These spent catalysts were studied in ex situ XANES, H_2-TPR and temperature programmed oxidation (TPO). For the TPO analysis, the deposited coke was investigated by continuous analysis of the evolved CO and CO_2

in a flow of synthetic air (20% O_2 in N_2). To this end, 50 mg of spent catalyst was degassed at 200 °C for 1 h under flowing Ar. Then, the catalyst was cooled down to room temperature and the TPO experiment was implemented with a heating rate of 10 °C.min^{-1} under 50 sccm of synthetic air and the effluent gas was analysed with an on-line FTIR. The details for the calculations of CO_x rate of formation and the weight percentage of coke are reported in S4. section of the Supplementary Information.

3. Results and Discussion

3.1. Atomic Layer Deposition of CrO_x on Silica

Aiming at the self-limited atomic layer deposition of chromium oxide on silica, a temperature range called ALD-window, wherein the $Cr(acac)_3$ precursor neither decomposes nor condenses, but reacts with silica surface hydroxyl groups called reactive chemisorption, was searched for. First, thermal behavior of the precursor was investigated with TGA-DTG and DTA analyses; See **Figure S.6 (a, b)**. The TGA-DTG curves indicate that $Cr(acac)_3$ almost completely vaporizes from about 170 °C to 305 °C, with a DTG peak centered at 284 °C, leaving only a minor amount of residue of less than 3 wt.%. The DTA curve indicates two endothermic peaks at 218 °C and 293 °C. The former peak is attributed to the simultaneous sublimation and melting of $Cr(acac)_3$. The next one, centered at 293 °C, originates from more vaporization, decomposition and reorganization of the remaining part of the precursor [35].

Then, the reaction of $Cr(acac)_3$ on SiO_2 surface was studied at different temperatures. During the $Cr(acac)_3$ reactive chemisorption step on silica surface -OH groups, Hacac was formed, concentration of which varied with $Cr(acac)_3$ dose sime (**Figure 2**). Inset of **Figure 2** shows the FTIR spectra of gases evolved from the ALD reactor at 120 min reactive chemisorption on silica at various temperatures. The Hacac peak intensity at 1625 cm^{-1} rises with temperature in the range of 170 to 200 °C, remains constant at 200 °C-230 °C, and again increases at 230-270 °C, at which additional peaks at 1740, 1760-1830 cm^{-1} for acetone, acetic acid and formic acid (See

Figure S.7 for their spectra) appear and their intensity increases with temperature. At higher substrate temperatures methane, CO and CO_2 were also detected, not reported here.

As shown in **Figure 2**, Hacac evolution showed a time delay at the begining of the reactive chemisorption stage of ALD. Researchers who study ALD on flat films, reported such a time delay and called “incubation time/effect”. They showed that nucleation, which is highly complex, is the main cause of the time lag. This phenomenon occurs at the initial cycles and depends on different paramerters including substrate functional groups, precursor properties and substrate temperature [19,36–39]. In ALD on porous supports for the synthesis of catalysts, recently such delay time was also reported for the initial stage of the reactive chemisorption step [40]. In present study, we evidenced the appearance of acetone and water as transient initial stage products during the incubation time with weak FTIR peak intensities, not shown in **Figure 2**. As reported by Zhuravlev [41], amorphous silica is energetically heterogeneous support, regarding its surface functional groups. The uneven distribution and concentration of the different types of silanol and siloxane groups, including internal, isolated, geminal and vicinal silanols and siloxane bridges, result in a variety of reactivities toward external agents like ALD precursors, as reported by Hu and Turner [42]. So, a few number of surface sites are capable of readily interacting with adsorbed precursor and initiate decomposition of the ligand, but then quickly deplete as the exposure of precursor proceeds. The lower temperature a substrate has, the higher incubation time it shows, in consistency with what has been reported by other researchers [38,43].

The slowly decreasing Hacac peak intensity with $Cr(acac)_3$ dose time in **Figure 2**, after a maximum, to about 1400 min for ALD at 230 °C implies the self-limiting reaction of $Cr(acac)_3$ with silica –OH groups. Detection of other hydrocarbon molecules at temperatures higher than 230 °C is the result of the activated dissociation and partial decomposition of the acac ligands [44–46] bounded to the surface via Cr centers, rather than re-adsorption and reaction of the

Hacac with the support. The Hacac vapor was passed through the bare silica at different support temperatures and the outlet gas was monitored by FTIR. The resulting spectra did not show any sign of decomposition of Hacac. Therefore, it was concluded that Hacac does not dissociate on silica surface groups, as reported by others [43,47] too. Therefore, the temperature range of 200-230 °C considered as a proper ALD window for reactive chemisorption, in contrast to either condensation at temperatures lower than 190 °C or decomposition at temperatures higher than 230 °C. It is necessary to note that the analysis of the outlet gas with GC/MS (See **Figure S.8**) also has shown that Hacac (m/z = 100, 85, 72, 58, 43 amu) is practically the only product of the reactive chemisorption of $Cr(acac)_3$ in the first half-cycle of ALD reaction after the incubation time. The lower limit of the temperature window, i.e. 200 °C, was chosen for the reactive chemisorption of $Cr(acac)_3$ on silica for all catalysts preparation.

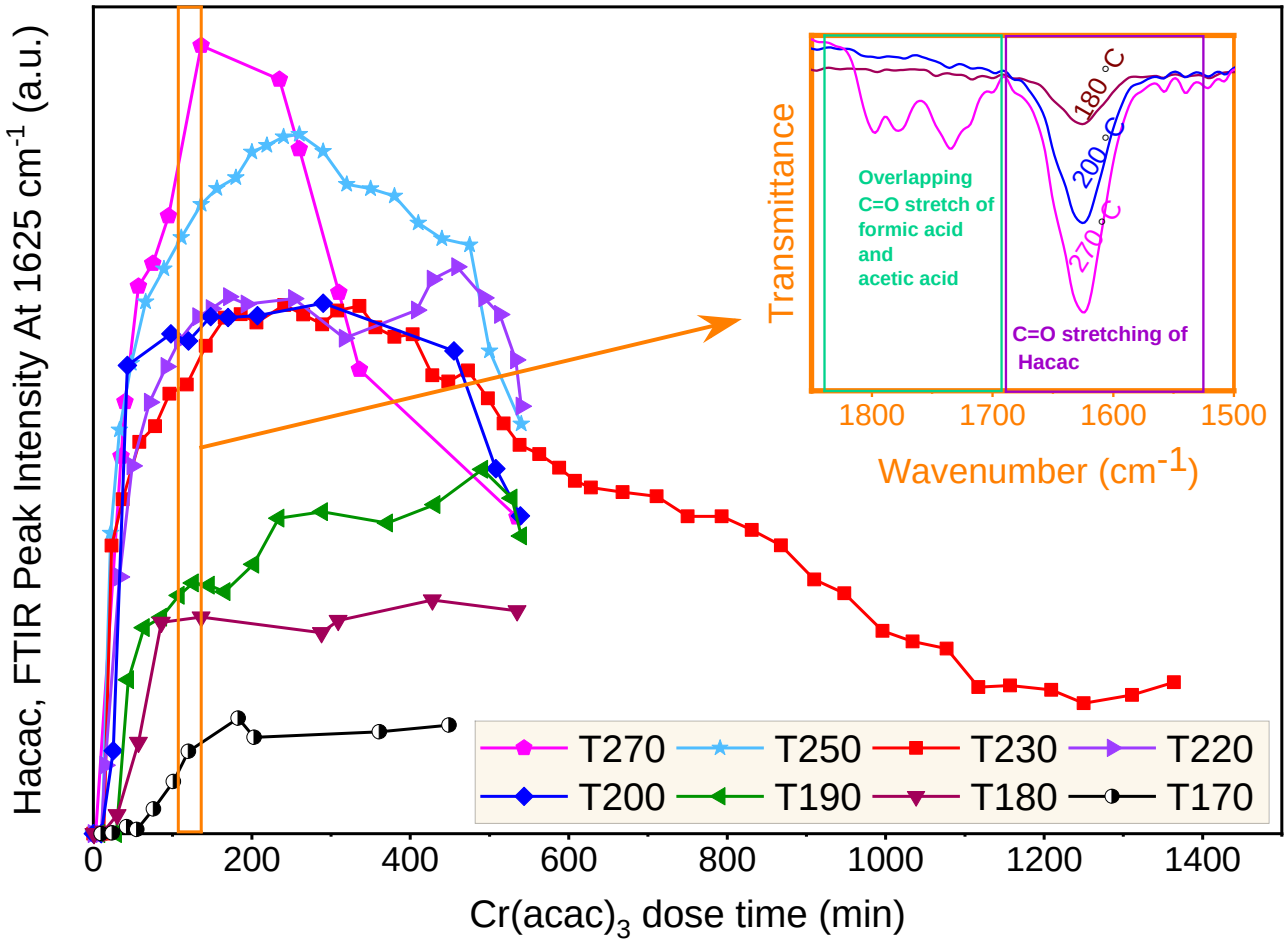

Figure 2. Hacac FTIR peak intensity at 1625 cm^{-1} measured as a function of $Cr(acac)_3$ dose time during the reactive chemisorption step. Inset: FTIR spectra of outlet gas at dose time of 120 min for various support temperatures

After purging the ALD reactor with Ar, as the third step of ALD, synthetic air was used for the oxidation of remaining ligands of the chemisorbed $Cr(acac)_x$. As presented in **Figure 3**, different carbonaceous components including acetone, acetic acid, methane, CO and CO_2 released during the ligands oxidation step. Removal of the acac ligands most likely took place through combustion reactions with a complex reaction mechanism related to the activation of O_2 molecules, insertion of O* into hydrocarbon chain of the ligands which might have been adsorbed with various configurations, C-C bond cleavage, various desorption modes of different dissociated hydrocarbon products, and deep oxidation of the hydrocarbon fractions [39,44].

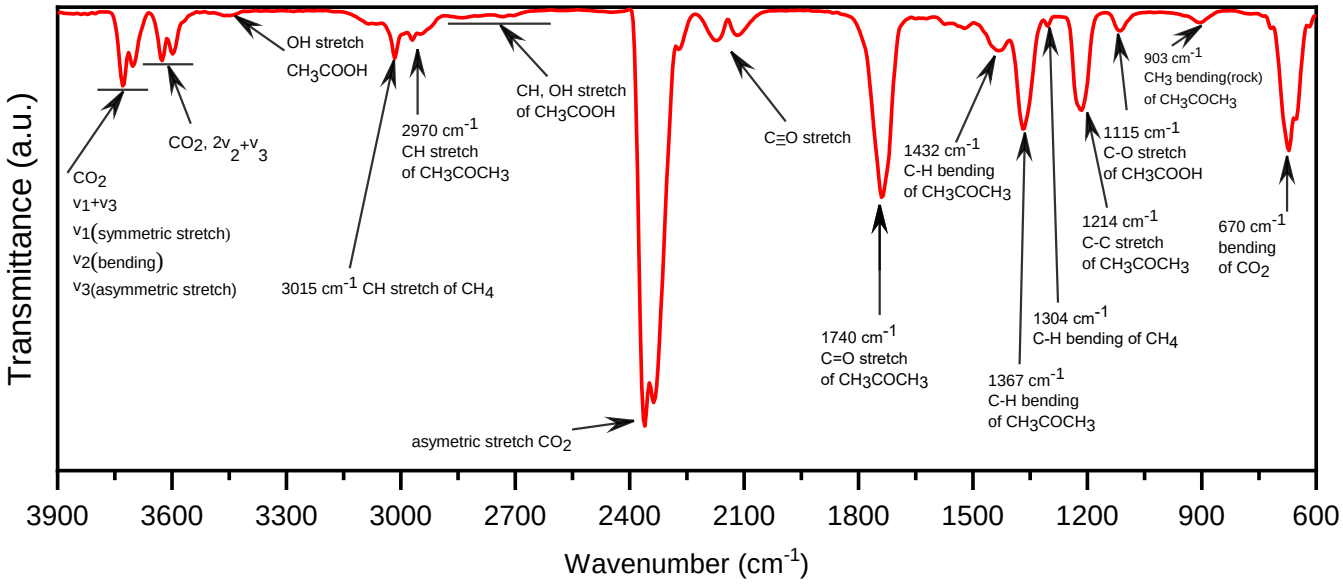

Figure 3. FTIR spectrum of oxidation of effluent gas from $Cr(acac)_x$ on silica formed during the first step in ALD cycle, at 5 min time on stream in the synthetic air

Figure 4 shows the Cr loading measured by ICP-OES as a function of reactive chemisorption dose time. Considering the density of surface –OH groups of silica support measured by Grignard method, 4.73 $OH.nm^{-2}$, the surface coverage of Cr species was also calculated and presented in **Figure 4**. Assuming a monolayer coverage in the first ALD cycle by complete consumption of surface –OH groups [48] or using the theoretical value of monolayer coverage of Cr, 1.61 $Cr.nm^{-2}$ [49], the results lead us to less than

12% monolayer coverage of silica by chromium oxide species. The sub-monolayer coverage stems probably from the lateral steric hindrance of organic ligands bound to the deposited Cr species and partial passivation and blocking of the surface groups by reaction products, i.e. adsorption of Hacac molecules on surface –OH groups [40,46,47]. However, additional evidences are needed to support this speculation.

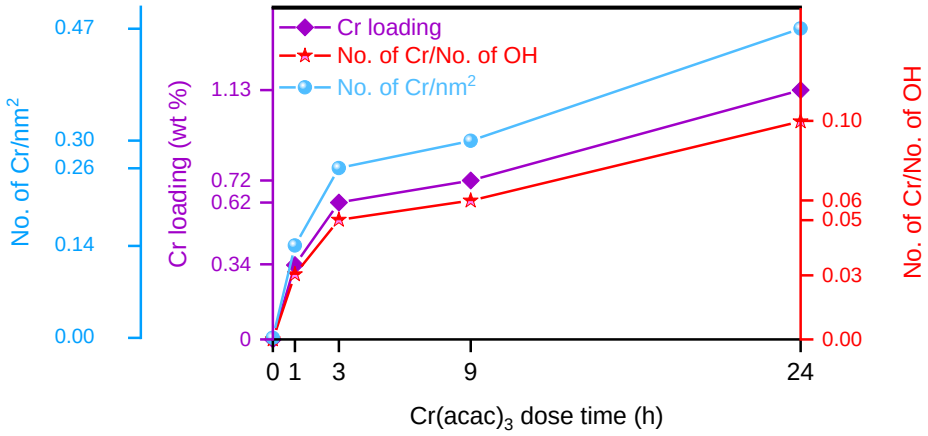

Figure 4. Chromium loading measured by ICP-OES and number of Cr per nm^2 of silica (left axes) and Cr molar surface coverage per number of moles of –OH groups on silica surface (right axis) as a function of $Cr(acac)_3$ dose time during the reactive chemisorption step in the first half ALD cycle at 200 °C.

3.2. Textural and Structural Characterization

Textural analyses by N_2 adsorption-desorption isotherms and the resulting pore-size distributions of catalysts presented in **Figure 5** (a, b). Results show the type IV isotherm and type H2 hysteresis which are associated with capillary condensation and desorption in open ended mesoporous structures of silica. Due to minor CrO_x loadings of both ALD and impregnated catalysts, all the samples showed similar behavior with the same surface area and average pore size values in the range of 243-259 $m^2.g^{-1}$ and 2.7 nm respectively.

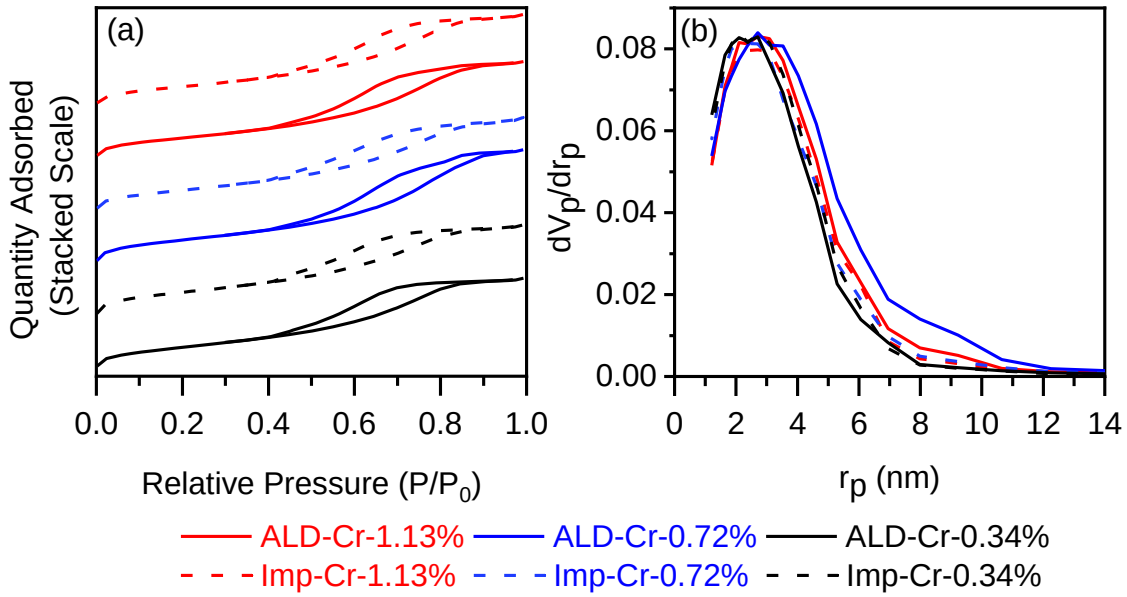

Figure 5. (a) N_2-adsoprtion-desorption isotherms and (b) pore-size distribution curve for ALD and impregnation catalysts

The study of crystalline structure of CrO_x/SiO_2 catalysts, by X-ray diffraction (XRD) method, only shows a single broad and strong peak of the silica support in the range of 2θ = 15-35 ° without any obvious diffraction peak of CrO_x species even for the sample with the highest chromium loading, before and after the CO_2-ODHP reaction **(See Figure S.9)**. This result, comes from the low content of chromium oxide and the small size of any possible crystals [11,50]. The FTIR spectra of catalysts was measured and represented in **Figure S.10, 11**. Bands at 1000 and 1250 cm^{-1} and a band at 750 cm^{-1} are related to vibrational motion of Si-O bonds and vibrations of Si next to bridging oxygen. Cr(VI)-O bond creates a weak band at 900 cm^{-1} which becomes larger by increasing the Cr loading as reported by Baek et al. [9].

The X-ray Absorption Near Edge Structure (XANES) for the K-edge of Cr was applied to study the oxidation state of Cr species and the dominant Cr form in each sample. Reference spectra were also collected from Cr_2O_3 and CrO_3 powder (See **Figure 6** and **Figure S. 12**). The CrO_3 spectrum shows a pre-edge peak at 5.994 keV that is the characteristic of Cr(VI) in a nearly perfect tetrahedral symmetry in lack of an inversion centre. This peak is assigned to the dipole allowed electron transition from the Cr 1s

orbital to an empty antibonding molecular orbital of Cr 3d in a tetrahedral field. In contrast, for the Cr_2O_3 reference, regarding the symmetry of Cr(III) in the octahedral coordination and the presence of an inversion centre, the 1s→3d transition is more difficult and therefore the pre-edge peak disappears. The edge position is another difference between these reference materials which is red-shifted with decreasing the oxidation state from Cr(VI) to Cr(III) and increasing the symmetry of the Cr centre [51–53]. The results of the XANES study of the catalysts show the presence of mix-valence of Cr in both series of samples where Cr(VI) is the dominating oxidation state.

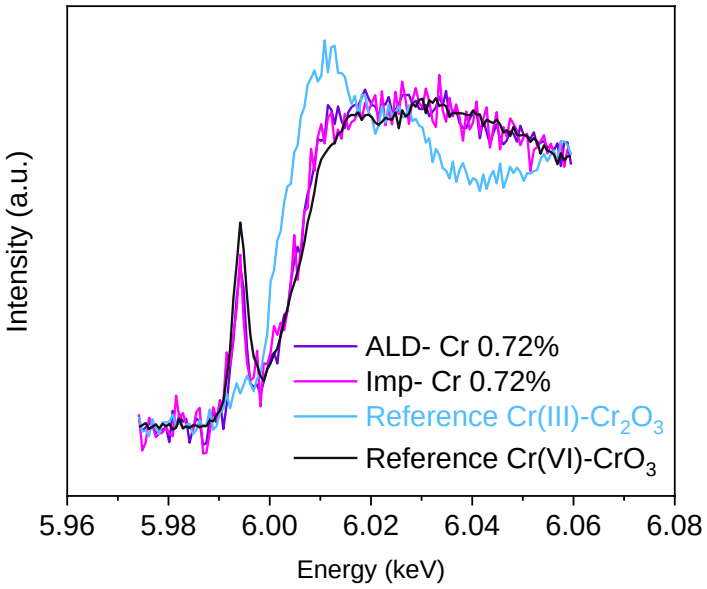

Figure 6. XANES spectra of reference model materials, as-synthesized ALD and impregnation catalysts with a Cr loading of 0.72 wt % recorded on Lab-Scale XANES instrument. XANES spectra of other catalysts can be found in **Figure S. 12**

UV-Vis diffuse reflectance spectra (UV-Vis DRS) were measured to assess the electronic structure, and distinguish different types of Cr oxides. As represented in **Figure 7 (a, b)**, all the samples indicate overlapping peaks from 200-1000 nm for ligand-to-metal charge transfer (LMCT) of different CrO_x species. As deconvoluted with Gaussian function, the two first peaks in the range of around 200-318 nm and 318-424 nm are the characteristics of charge transfer in the monomeric Cr^{6+} oxides with a tetrahedral symmetry. The third peak around 424-535 nm represents the distortion of the isolated Cr^{6+} oxides as a result of polymerization. The next peak

around 535-700 nm was assigned to the tiny octahedral Cr_2O_3 crystals. The last peak around 700-1000 nm is reported as an indicative of Cr_2O_5 in quare pyramidal or distorted tetrahedral crystals **(See Table S. 5)** [8,11,14,54–56].

From **Figure 7 (a, b),** we realize that the ALD and impregnation samples of this work have a combination of Cr^{6+} in the form of mono/poly chromates and CrO_x surface crystals. By deconvolution of the spectra, as shown in **Figure 7 (c)**, we find that the polychromate species have higher density in ALD catalysts compared to impregnation ones.

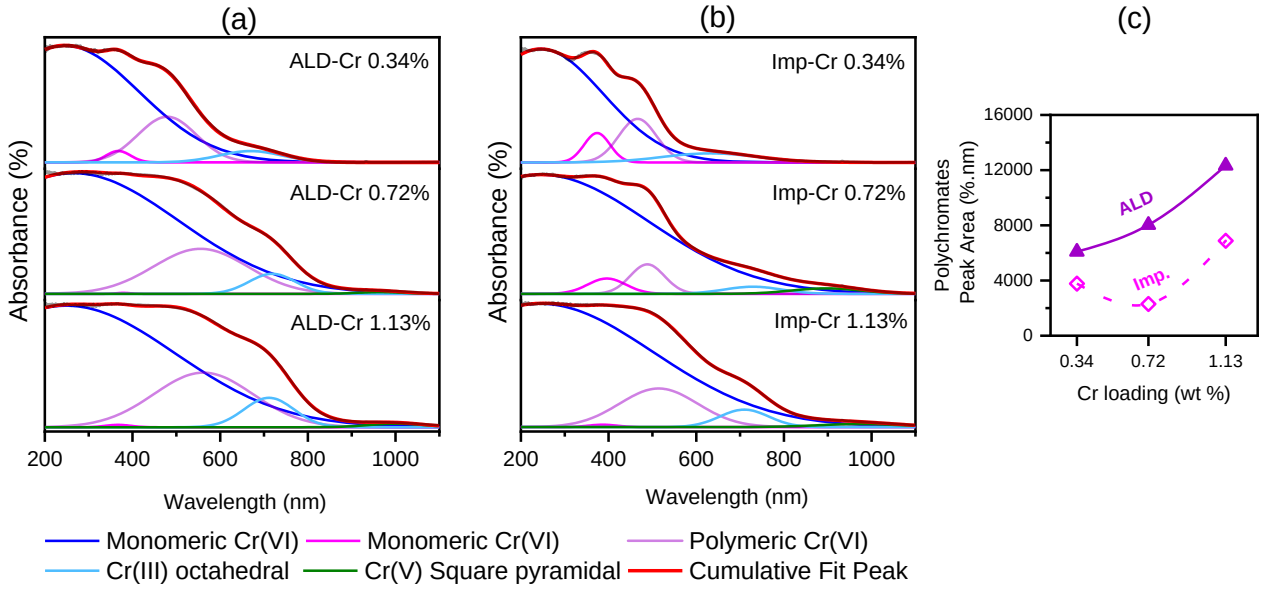

Figure 7. (a, b) UV-Vis DRS spectra with their deconvolutions for ALD and impregnation catalysts in absorption mode. **(c)** Comparing the peak area of polychromates of ALD and impregnation catalysts in each Cr loading.

Raman spectra of ALD and impregnation catalysts were presented in **Figure 8** and **Figure S.13, 14**. In Raman spectrum of CrO_x/SiO_2 catalysts, di-oxo $(O=)_2Cr(\text{-}O\text{-}Si)_2$ and mono-oxo $O=Cr(\text{-}O\text{-}Si)_4$ show bands at 980 and 1000 cm^{-1} [9]. The dominant form of chromium oxide in both series of catalysts is the di-oxo chromate not mono-oxo chromate. Further, ALD catalysts, in opposite to their impregnation counterparts, have shown a distinct band around 270 cm^{-1}, assigned to polymerized $Cr(VI)O_x$ [14]. Additionally, Si-O-Si asymmetric stretch, Si-O-Si symmetrical stretching, network bending modes and longitudinal-optical silica network show peaks in 1065, 800, 390, and 1150 respectively [14,57].

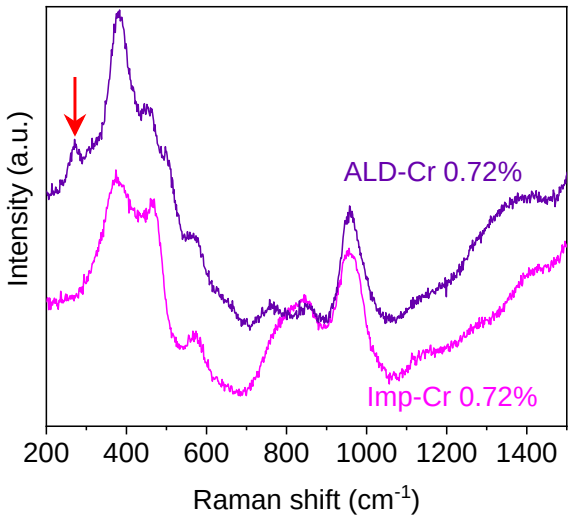

Figure 8. Raman spectra of ALD and impregnation synthesized catalysts with Cr loading of 0.72 wt %. The laser wavelength of Raman microscope was 457 nm.

Then, we studied the samples with HRTEM/STEM-HAADF and their EDS mapping. **Figure 9** and **Figure 10**, respectively show the images of ALD and impregnation catalysts with Cr loading of 0.72 wt %. As shown in **Figure 9 (a, b, e, f)**, the ALD-synthesized catalyst is made of small and highly dispersed chromium oxide particles. Ideally the ALD method results in a conformal and uniform layer-by-layer deposition. However, in the initial cycles of most growth modes of ALD, instead of a uniform layer, dispersed ultra-small 2D clusters of surface species are formed. In the oxidation step and the subsequent heat treatment of the catalyst, the sintering of the surface clusters and the creation of 3D amorphous particles, but still small and highly dispersed particles, occur [58–60]. As represented in **Figure 7(c)**, the UV-Vis DRS show the higher content of poly-chromates in the ALD catalysts with the higher degrees of polymerization compared to their corresponding dry impregnation catalysts. Therefore, the resulting ALD synthesized highly dispersed small CrO_x particles, as reported in literature [8,14], are mainly made of poly-chromates with different degrees of polymerization. Beside these highly dispersed amorphous surface CrO_x particles, the formation of isolated mono-chromate species and the weak crystalline layers of chromium oxide is also confirmed by UV-Vis DRS, HRTEM images (**Figure 7 (a)** and **Figure 9 (c, d)**).

In contrast, as can be seen in **Figure 10**, the dry impregnation method has produced mostly large particles of the chromium oxide. In this synthesis method, based on the literature [61,62], the drying and calcination procedure, decompose the chromium nitrate hydrate to O_2, N_2O and NO_2 and cause the severe redistribution and sintering of chromium oxides. This way, relatively higher population of the large crystalline particles of chromium oxide are formed (See **Figure 10 c, d**). However, as represented in the UV-Vis DRS (**Figure 7 (b)** of the manuscript), the formation of smaller amorphous poly-chromates and the mono-chromate species, cannot be excluded.

The crystalline structure of ALD and impregnation catalysts (See **Figure 9 (c, d)** and **Figure 10 (c, d)**) has interplanar spacings of 0.35 and 0.27 nm. These lattice spaces are in match with orthorhombic CrO_3 reported in X'Pert HighScore Reference Patterns numbers of 01-073-1547, 00-007-0228 and 00-001-0622.

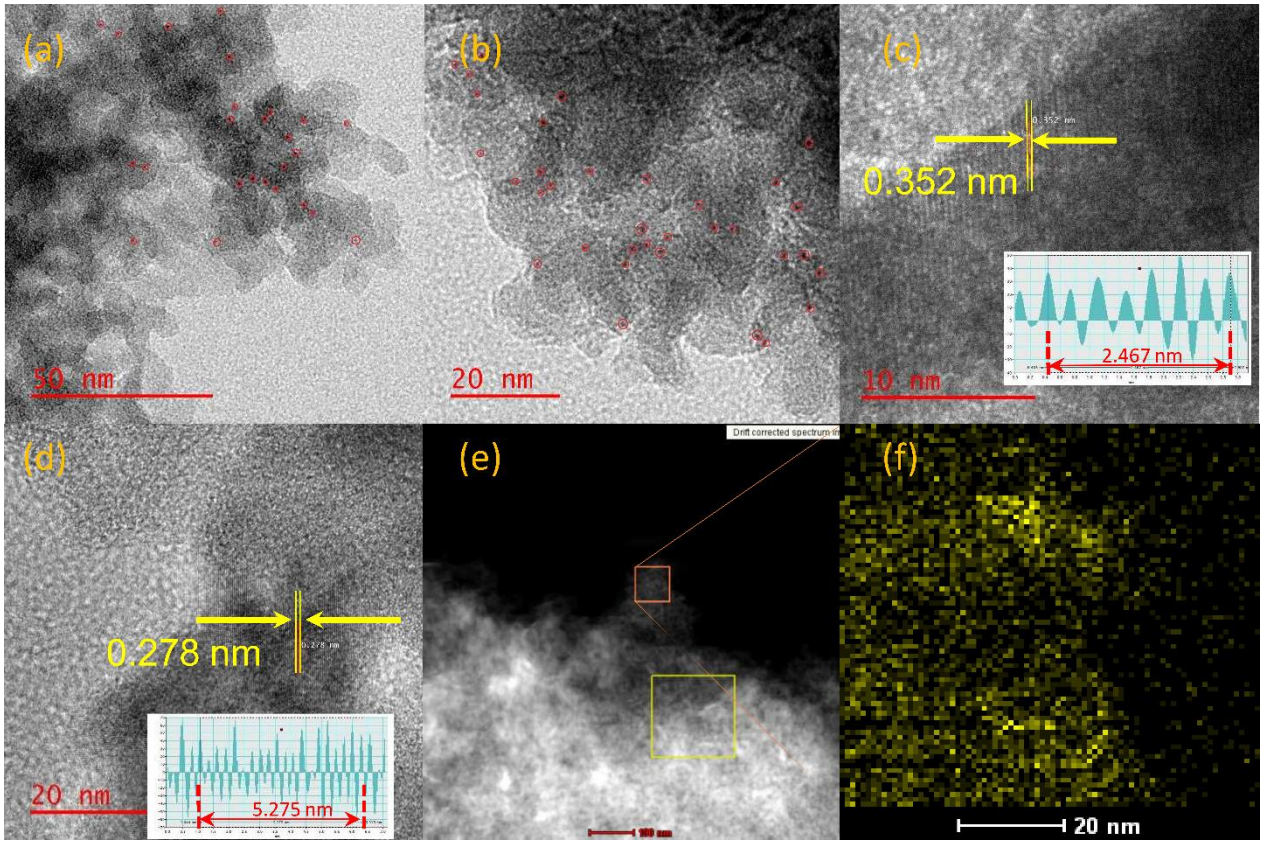

Figure 9. ALD catalyst with Cr loading of 0.72 wt %. (a, b) High resolution transmission electron microscopy (HRTEM) images of CrO_x particles and (c, d) crystalline structure of chromium oxide. Red circles highlight few of the many CrO_x particles. (e, f) Scanning transmission electron microscopy image in high angle annular dark field

mode (STEM-HAADF) with the corresponding energy dispersive X-ray spectroscopy elemental mapping images of Cr. Insets in (c) and (d) represents the IFFT profile of the observed lattice fringes for the d-spacing calculations.

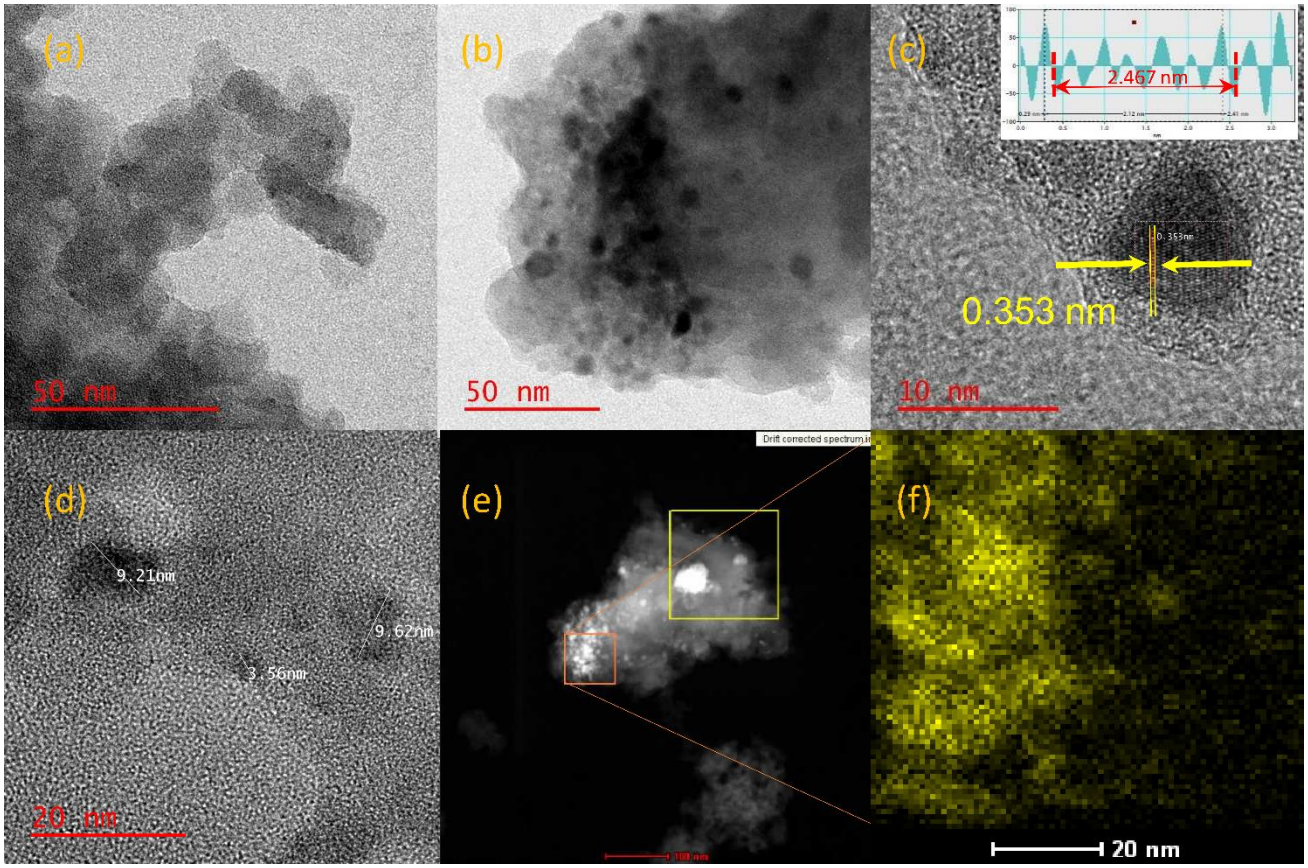

Figure 10. Impregnation catalyst with Cr loading of 0.72 wt %. (a, b) High resolution transmission electron microscopy (HRTEM) images of CrO_x particles and (c, d) crystalline structure of chromium oxide. (e, f) Scanning transmission electron microscopy image in high angle annular dark field mode (STEM-HAADF) with the corresponding energy dispersive X-ray spectroscopy elemental mapping images of Cr. Inset in (c) represents the IFFT profile of the observed lattice fringes for the d-spacing calculations.

Temperature programmed reduction (TPR) was examined to study the reducibility of the catalysts. **Figure 11** (a, b) shows the H_2 consumption as a function of temperature for ALD and impregnation catalysts. The H_2-TPR of CrO_x/SiO_2 catalysts exhibits a major peak around 450 °C, minor broad peaks around 250 °C, and 700 °C and a shoulder around 350 °C. The peaks were assigned to reduction of Cr^{6+} with different sizes to Cr^{3+} for peaks below 600 °C and Cr^{3+} to Cr^{2+} for the region higher than 600 °C [11,34,63,64]. As shown in **Figure 11** (c), the ALD samples show a higher degree of reducibility with higher TPR peak area at temperatures lower than 600 ^oC, compared to the analogous impregnation samples. Going over several publications, we

found some controversies in the assignment of H_2-TPR peaks. Some researchers believe that the isolated chromium oxide species are highly inactive and have a reduction peak at very high temperatures, while polymeric CrO_x species show about 200 ^oC lower temperature peak [16]. Some others assign the major peak in H_2-TPR to the monochromate in the form of isolated mono-oxo and di-oxo chromium oxides [65]. Another group shows the absence of any mono-oxo chromium oxide over the silica support. they refer some of the overlapping H_2-TPR peaks to the formation of polychromate species in presence of H_2O during the TPR reaction [57]. Considering the UV-Vis DRS and Raman results, we may agree with the last group in considering the water catalysed formation of polychromate during the H_2-TPR reaction and reduction of these newly formed species in parallel to the isolated species. Therefore, the main outcome of these H_2-TPR data is the uncovering of more reducibility of ALD catalysts compared to their analogous impregnation counterpart.

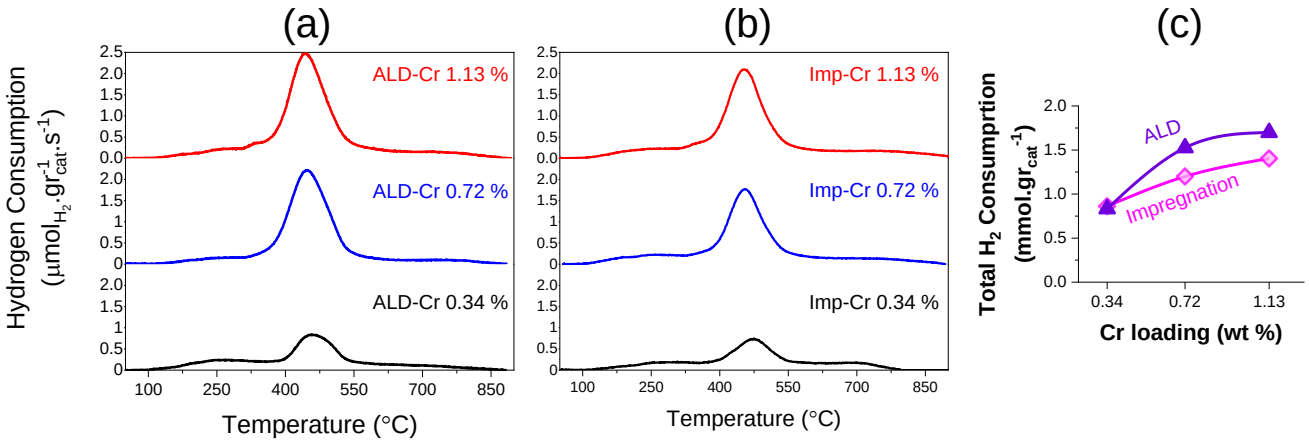

Figure 11. H_2-TPR of as-synthesized (a) ALD and (b) Impregnation CrO_x/SiO_2 catalysts, at a heating rate of 10 $^oC.min^{-1}$ under 8 sccm of 7% H_2 in Ar. (c) Total H_2 consumption of ALD and impregnation catalysts as a function of Cr loading

NH_3 was selected as an appropriate probe molecule to study both the dispersion and the acid properties of catalysts in the TPD method (**Figure 12a, b**). As shown, the total area of NH_3-desorption peaks intensifies with the increasing of chromium loading. The ALD catalysts have up to 2 times higher amounts of NH_3-desorption indicating the higher

dispersion of Cr oxides, compared to the impregnated catalysts. NH_3-TPD of all the samples shows broad peaks in the range of 120-600 °C, resulting from the overlapping of weak (α peak), medium (β peak) and strong (γ peak) acidic sites, in line with what was reported in literature [12,66]. These peaks were separated by mathematical deconvolution method using Gaussian function and the results were shown in **Figure 12c**. This figure shows that, for all catalysts, the amount of medium acid sites is greater than the weak and strong acid sites. About the relation of NH_3-desoprtion and catalytic activity, literatures show that the medium acid sites (β peaks) are responsible for the conversion of propane in CO_2-ODHP [13]. **Figure 12c** shows that the ALD catalysts have higher β-peak which results in their higher activity in the catalytic performance tests. The last peak that appeared for the samples with 0.34 wt.% of Cr, which is not used in the bar charts of **Figure 12c**, may originate from the dehydroxylation of the support around the calcination temperature as reported by Matveyeva et al. [67].

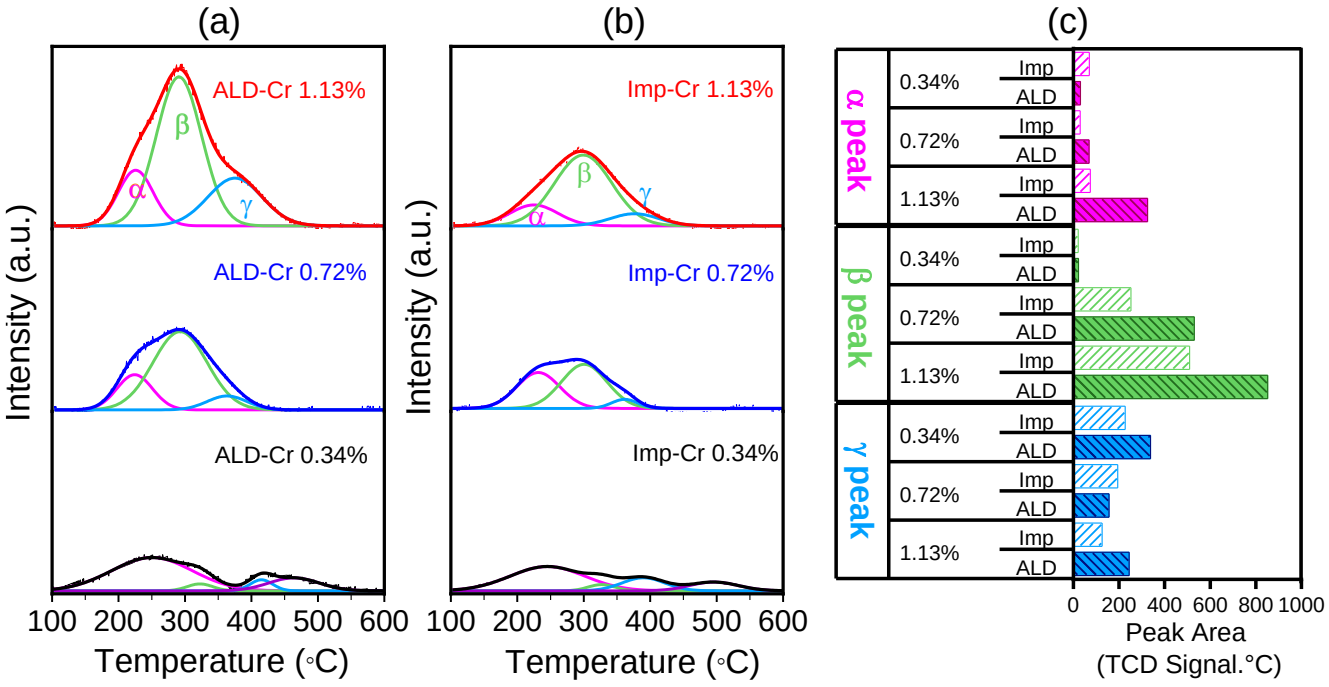

Figure 12. NH_3-TPD of (a) ALD and (b) impregnation catalysts with different Cr loadings. (c) The α, β, γ peak area values for each kind of acid sites as a function of Cr loading for ALD and impregnation catalysts.

3.3. Catalytic Activity

Figure 13 (**a**, **b** and **c-f**) illustrates the time on stream (TOS) propane conversion, specific reaction rate and selectivity of respectively propylene, methane, ethane and ethylene for the ALD and impregnation catalysts. The change in the number of moles of the products with TOS are represented in **Figure S .15.** The ALD catalysts exhibited up to 18%, 15% and 1.8 times higher conversion, yield of propylene and specific reaction rates, respectively, in comparison to the impregnation ones. In both series of catalysts, the conversion values were increased with Cr-loadings. According to the previous observations [7,66,68–70] it is generally suggested that CO_2-ODHP reaction over chromium oxide catalysts occurs through two different redox and non-redox pathways. In the redox pathway, CO_2 directly participate in the reaction mechanism through Eq. 5:

$$C_3H_8 + CO_2 \rightarrow C_3H_6 + CO + H_2O \qquad \text{Eq. 5}$$

In which the lattice oxygen of chromium oxide takes part in the reaction and the CO_2 re-oxidizes the reduced chromium species in the Mars van Krevelen (MvK) mechanism (Eq. 6, 7) [9]:

$$C_3H_8 + CrO_x \rightarrow C_3H_6 + CrO_{x-1} + H_2O \qquad \text{Eq. 6}$$
$$CO_2 + CrO_{x-1} \rightarrow CO + CrO_x \qquad \text{Eq. 7}$$

Regarding the role of CrO_x in this redox reaction, there are mainly two different speculations. Some researchers believe that Cr^{6+} and Cr^{3+} are the main redox couples. Some others have shown that Cr^{3+}/Cr^{2+} redox species take part in the dehydrogenation. In this regard, it seems that at the beginning of the reaction, reduction of Cr^{6+} to Cr^{3+} is prominent and after a while the reduction of Cr^{3+} to Cr^{2+}, which are formed from Cr^{6+}, becomes more relevant [7,34,51].

In the non-redox pathway, propane is directly dehydrogenated over CrO_{x-1} and CO_2 removes the produced hydrogen through reverse water-gas shift reaction (RWGS) to increase the propylene yield (Eq. 8, 9) [7,68,69]:

$$C_3H_8 \rightarrow C_3H_6 + H_2 \qquad \text{Eq. 8}$$
$$CO_2 + H_2 \rightarrow CO + H_2O \qquad \text{Eq. 9}$$

The RWGS products can also help the desorption of ethylene that possibly is produced by either the dry reforming or thermal/catalytic-cracking reactions (Eq. 10 to 12) [7,68,69].

$C_3H_8 + 3CO_2 \rightarrow 6CO + 4H_2$ Eq.10

$2C_3H_8 + 2CO_2 \rightarrow 3C_2H_4 + 2CO + 2H_2O$ Eq.11

$C_3H_8 \rightarrow C_2H_4 + CH_4$ Eq.12

From the TOS curves, we recognize that at the beginning of the reaction, CO, methane and ethylene have higher values. As the reaction proceeds, the number of moles and selectivity of these byproducts decreases. Therefore, we propose that at the beginning of the reaction, that the catalysts have more Cr(VI), the conversion of propane and the amount of byproducts are high. By the progress of the reaction with TOS, the number of less selective sites decreases which results in higher selectivity of propylene.

However, interaction of propane and CO_2 over chromium oxide catalysts is not limited to the aforementioned reactions. The other role of CO_2 in the CO_2-ODHP reaction is elimination of coke, as the product of severe cracking reactions, through reverse Boudouard reaction (Eq. 13) [7,68,69,71].

$CO_2 + C \rightarrow 2CO$ Eq.13

Based on the UV-Vis-DRS, HRTEM and dark field STEM images, TPR and NH_3 desorption results, the ALD catalysts revealed the higher dispersion of CrO_x particles and higher content of polymeric Cr(VI) species, compared to their analogous impregnation catalysts. This aspect of ALD synthesized catalysts, resulted in their higher activity and reaction rates. In contrast, the lower dispersion and higher ratio of inactive monomeric Cr(VI) in the impregnated catalysts decreased their activity in dehydrogenation of propane with CO_2. As reported by Jian Wang et al. [14], the polymerized chromium oxide species more strongly adsorb propane which results in higher conversion. The higher the degree of polymerization, results in the enhanced conversion of propane. The positive effect of dispersion of CrO_x particles on silica support in providing superior catalyst activity in CO_2-ODHP reaction was reported by Hao-Miao Wang and colleagues [13].

The study of catalytic performance with temperature was carried out in the temperature range of 550 °C to 700 °C. As shown in **Figure 14 (a, b)** and **Figure S.16** with the increase of temperature, the selectivity of propylene dramatically decreases while the conversion of propane increases. At lower temperatures, e.g. 550 °C and 600 °C, the selectivity (and number of moles) of methane and ethylene is not significant while propylene and CO are the major products. Regarding the number of moles of propylene compared to CO, we realize that propylene has higher values for the ALD and impregnation catalysts with Cr loadings of 0.72 and 1.13. Therefore, the direct dehydrogenation of propane partly occurs over these catalysts in parallel to the redox pathway. As the temperature increases from 600 °C to 700 °C, the number of moles of CO, methane and ethylene as dry reforming/cracking reaction products increases and the selectivity of propylene decreases.

Results of blank test over silica powder shows a very small contribution of non-catalytic reactions at 600 °C. However, as the temperature increases, the extent of non-catalytic reactions, in agreement with [72], also increases with a lower selectivity of propylene.

To calculate the kinetic parameters from these data, we modelled the reactor with a plug flow reactor (PFR), as the frequently quoted rule with $L/d_p>30$ [73] was met. A power-law reaction rate model was assumed with the order of 0.65 with respect to propane reported for CO_2-ODHP over silica supported chromium oxide catalysts [68]. Since excess CO_2 ($CO_2/C_3H_8 = 5$) was used in the CO_2-ODHP reaction, the CO_2 concentration in the reactor remained almost constant. Therefore, the rate constant at each temperature was calculated in the temperature range of 550-700 °C. The Arrhenius plots were presented in **Figure 14c** and the resulting k_0, E_a and the R^2 values were presented in **Table 1.** As shown, the slopes of the curves do not change and the apparent E_a in the temperature range of 550-700 °C were in the range of 95-133 $kJ.mol^{-1}$ in agreement with reported values [74,75]. Further, the Mears and Weisz-Prater criteria and Biot number calculations

according to literature [76–78] (See the **S. 9 section** of Supplementary Information) indicate that the heat and mass transfer effects on the reaction kinetics are negligible in the whole temperature range. Therefore, the kinetics is not falsified with the transfer limitations and true activation energies are obtained.

Table 1. Activation energy (Ea), R^2 and pre-exponential factor (k_0) for the ALD and impregnations catalysts with different Cr loadings

	E_a (kJ.mol^{-1})		R^2		k_0[1]	
%Cr	**ALD**	**Imp**	**ALD**	**Imp**	**ALD**	**Imp**
0.34	115	119	0.992	0.989	1.5	1.6
0.72	94	105	0.989	0.993	0.2	0.6
1.13	96	95	0.988	0.982	0.3	0.2

[1] (mol$^{0.65}$. m$^{-1.95}$.gr-cat^{-1}.s^{-1})

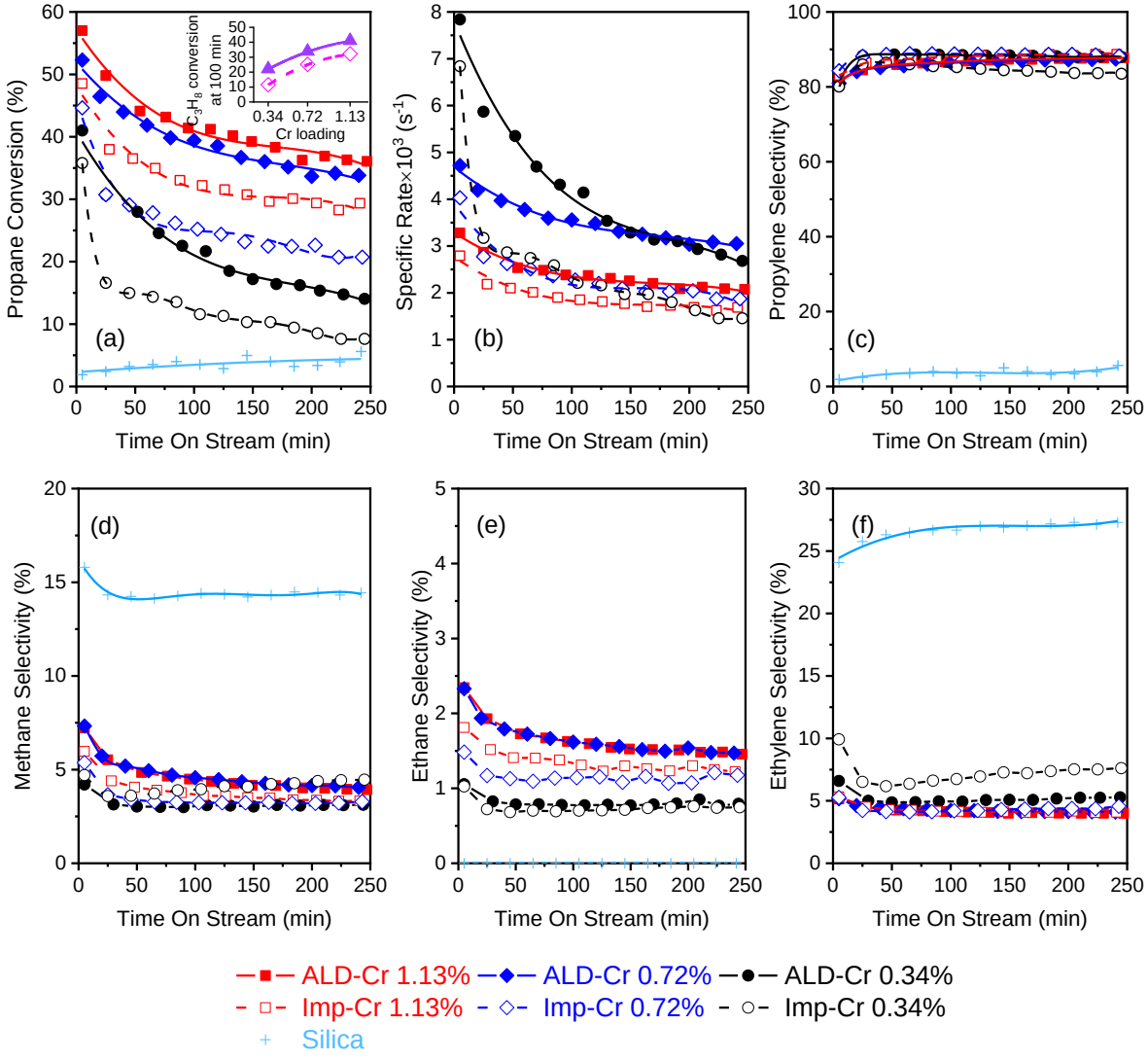

Figure 13. (a) Conversion of propane, (b) specific reaction rate and (c, d, e, f) selectivity of propylene, methane, ethane and ethylene respectively for dehydrogenation of propane in presence of CO_2 as a function of time on stream (TOS). Inset in (a): the propane conversion as a function of Cr loading at 100±5 min TOS for ALD and Impregnation catalysts. Reaction conditions: T = 600 °C, total flow rate = 30 sccm, C_3H_8 = 1.5 sccm, CO_2:C_3H_8 = 5:1.

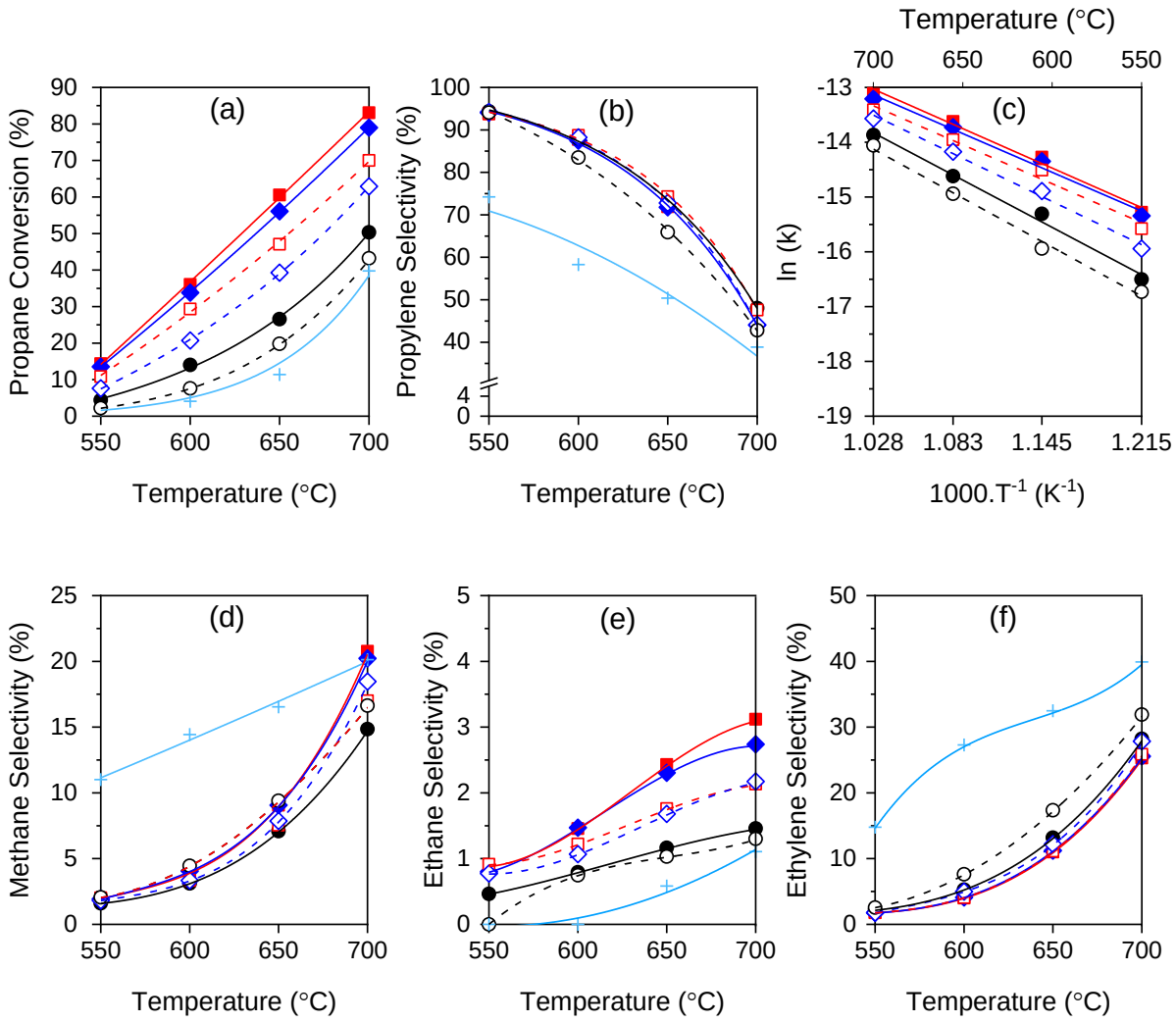

Current colors, types and markers are the same as in Figure 13

Figure 14. (a) Conversion of propane vs temperature, (b) selectivity of propylene as a function of reaction temperature, and (c) Arrhenius Plot of ln(k) vs $1000.T^{-1}$ (K^{-1}), (d, e, f) temperature dependence selectivity of methane, ethane and ethylene respectively. Reaction condition: Total flow rate = 30 sccm, C_3H_8 = 1.5 sccm, CO_2:C_3H_8 = 5:1.

3.4. Catalysts Deactivation

To find out the reason of the activity loss with time on stream, reported in **Figure 13** of **Section 3.3.**, XANES spectra of spent catalysts were measured and represented in **Figure 15 (a, b)**. The results show the disappearance of Cr(VI) pre-edge peak and edge

red-shift as clear signs of conversion of Cr^{6+} to Cr^{3+} upon introduction of the CO_2-ODHP reaction feed, in accordance with what was reported by Kumar et al. [53].

Then, to study the changes of reducibility of the catalysts after reaction and re-oxidation, TPR was performed on reoxidized catalysts, as shown in **Figure 16** and **Figure S17 (c-f).** The ALD catalysts presented higher reducibility with minor changes, in comparison to the fresh samples, while the impregnation catalysts showed a considerable loss of reducibility and a high temperature TPR peak. These results suggest that for the ALD catalysts, with higher proportions of polymerized Cr species, the reduction of Cr^{6+} to Cr^{3+} was more reversible than that of impregnation catalysts.

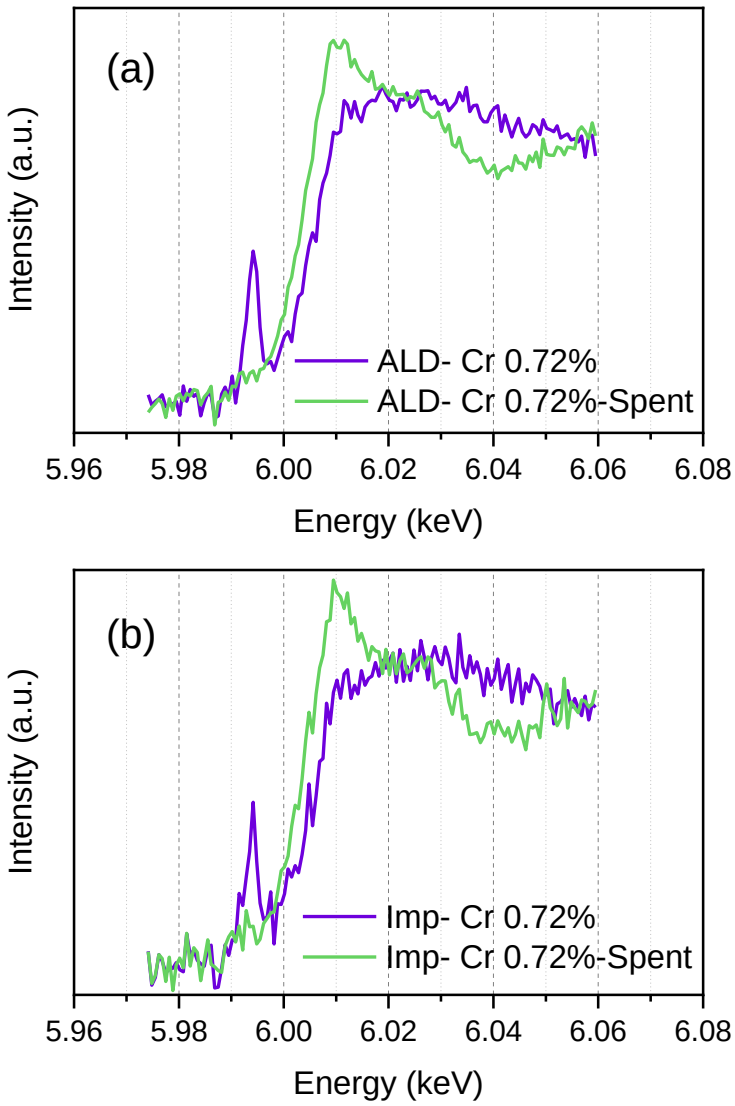

Figure 15. XANES spectra of as-synthesized and spent (a) ALD and (b) impregnation catalysts with Cr loading of 0.72 wt %. The pent catalyst was collected after 6 h time on stream under CO_2-ODHP reaction at 600 °C with total flow rate of 30 sccm, C_3H_8 = 1.5 sccm, CO_2:C_3H_8 = 5:1

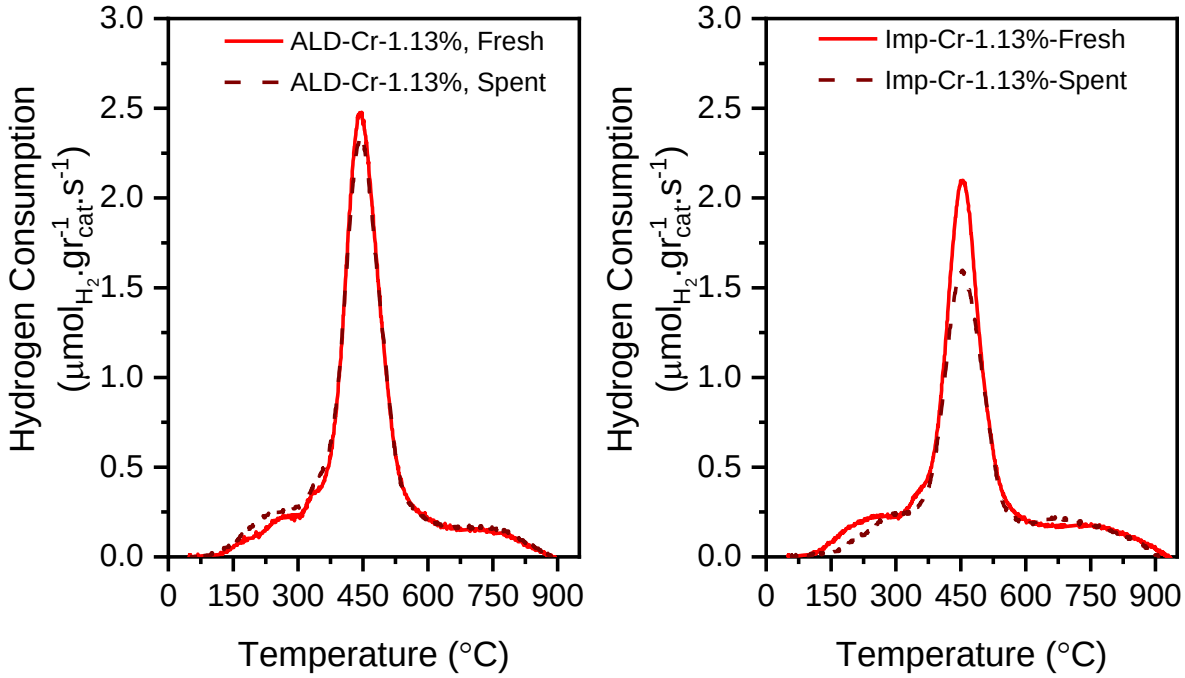

Figure 16. H_2-TPR spectra of as-synthesized and spent (a) ALD and (b) impregnated catalysts with Cr loading of 1.13 wt %. H_2-TPR reaction condition: heating rate = 10 °C.min^{-1}, 8 sccm 7% H_2 in Ar. The spent catalyst was collected after 6 h time on stream under CO_2-ODHP reaction at 600 °C with total flow rate of 30 sccm, C_3H_8 = 1.5 sccm, CO_2:C_3H_8 = 5:1 and then regenerated with 4% O_2 in N_2 at 550 °C for 1 h before TPR experiment. The whole set of data can be found in **Figure S.17**.

Further, the widely used temperature programmed oxidation (TPO) technique was utilized to quantify and measure the coke content of the spent catalysts that is the other cause for deactivation [79]. **Figure 17 (a, b)** shows that oxidized carbon atoms evolve dominantly as CO_2. This observation is supported by the thermodynamic consideration that CO_2 is the energetically favored product of TPO, and by the kinetic view that CO can be rapidly oxidized to CO_2 [80].

Figure 18 shows that the amount of coke deposits increases significantly with the increment of the chromium loading, while the relative deactivation rate has a reversed trend. In addition, the ALD samples that showed the higher activity in the CO_2-ODHP reaction exhibited higher amount of coke and less relative deactivation rate compared to the analogous impregnated catalysts.

From the results, firstly, we can deduce that the Cr(VI) oxide are responsible for more conversion of propane and the stronger adsorption of propane and propylene which causes cracking reactions and coke formation at the early stage of deactivation with a steep slope. Secondly, coke can selectively deactivate less-selective catalytic sites as reported by others [14,81–83]. As the selectivity enhancement is observed in **Figure 13** at the beginning of each TOS curve, the idea of less-selective site coating with coke may be rational. As can be seen in the TOS results (**Figure 13**), by the progress of the reaction, the deactivation of the catalysts proceeds with a low and ever-decreasing slope. This deactivation step may come from segregation or sintering of the surface chromium oxide sites as reported by Baek et al. [9]. The lower deactivation rate at the later TOS, which means more stability, may originate from another beneficial effect of coke that geometrically puts restriction on the sintering of CrO_x particles by isolating them from their proximate particles, as reported by Galsson et al. [84].

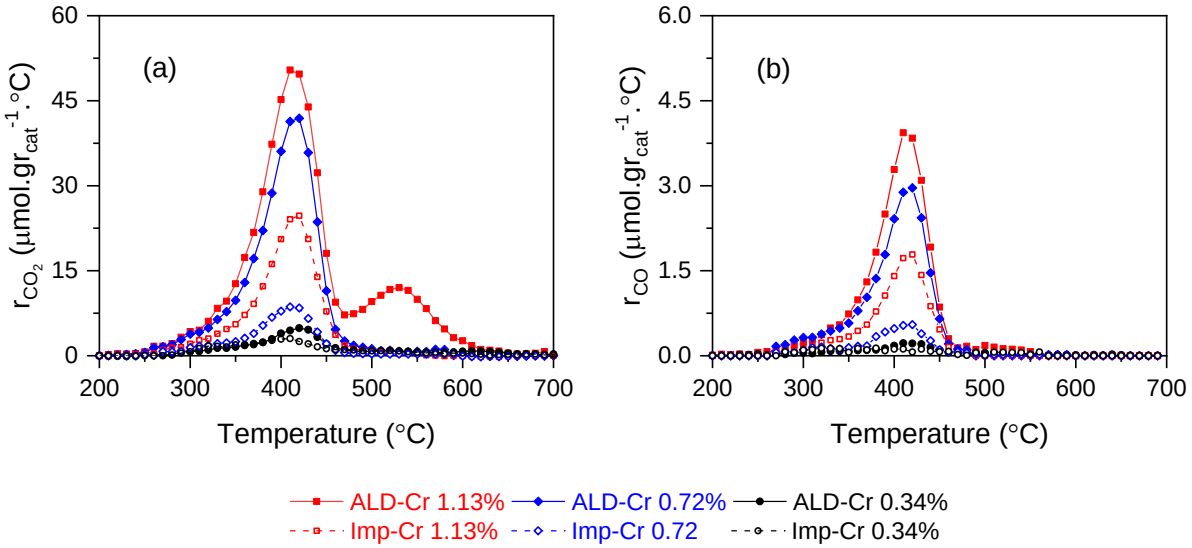

Figure 17. The rate of CO_2 and CO evolution as the only hydrocarbon products of Temperature Programmed Oxidation (TPO) reaction. TPO conditions: heating rate = 10°C.min^{-1}, air flow rate = 50 sccm, Before TPO, the catalysts were exposed to CO_2-ODHP reaction feed for 6 h TOS with a flow rate of 30 sccm at 600°C where the ratio of Ar: CO_2: Propane was 14:5:1.

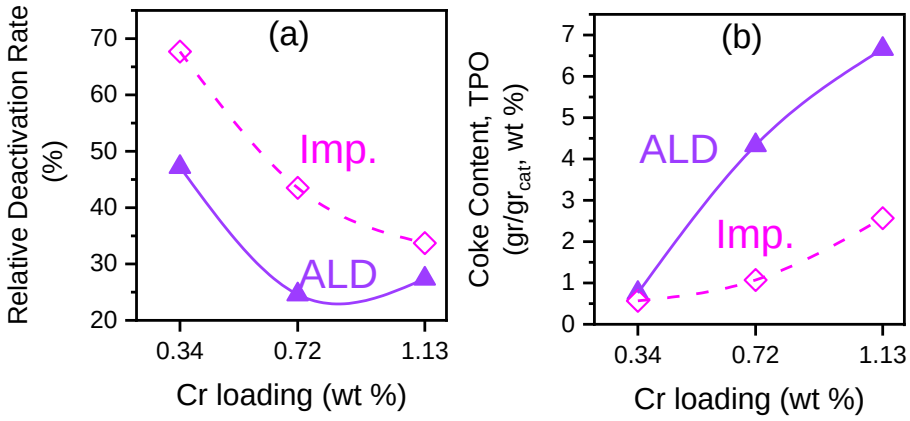

Figure 18. The relative deactivation rate calculated from conversion-TOS data **(a)**, coke content calculated from TPO curves **(b)** as a function of Cr loading in ALD and impregnation catalysts

4. Conclusion

In summary, the atomic layer deposition method was used to synthesize CrO_x/SiO_2 catalysts for dehydrogenation of propane with CO_2 to propylene (CO_2-ODHP). The ALD temperature window at which partial monolayer of reactively chemisorbed $Cr(acac)_3$ was formed on the silica, rather than the condensation or chemical vapor deposition, was found. The ALD synthesis method resulted in the higher dispersion of chromium oxide particles and higher content of polychromate species which both resulted in higher specific reaction rates in CO_2-ODHP reaction, while the selectivity did not drop significantly. We suggest that the higher activity in CO_2-ODHP reaction, acidity, and H_2-reducibility of the ALD catalysts result from the higher dispersion of CrO_x particles and enhanced contents of polychromates. In addition, the beneficial effects of coke on chromium oxide catalysts in CO_2-ODPH were observed in this study. The deactivated ALD catalysts with higher coke contents still show higher activity than the impregnation ones, due possibly to selective deactivation of less-active sites or the coke is not the main cause of the deactivation.

Funding

Partial financial support from Iranian National Science Foundation (INSF) under Contract No. 97015267 is gratefully acknowledged. A financial support from “Catalysts and Nano-structured

Materials" Scientific Chair of Iranian National Science Foundation (INSF ID 950020) is highly appreciated. S.H. was supported by the Academy of Finland (grant no. 295696).

References

[1] T. Otroshchenko, G. Jiang, V.A. Kondratenko, U. Rodemerck, E. V. Kondratenko, Current status and perspectives in oxidative, non-oxidative and CO2 -mediated dehydrogenation of propane and isobutane over metal oxide catalysts, Chem. Soc. Rev. 50 (2021). https://doi.org/10.1039/D0CS01140A.

[2] E. Gomez, B. Yan, S. Kattel, J.G. Chen, Carbon dioxide reduction in tandem with light-alkane dehydrogenation, Nat. Rev. Chem. 3 (2019). https://doi.org/10.1038/s41570-019-0128-9.

[3] E. Gomez, S. Kattel, B. Yan, S. Yao, P. Liu, J.G. Chen, Combining CO2 reduction with propane oxidative dehydrogenation over bimetallic catalysts, Nat. Commun. 9 (2018). https://doi.org/10.1038/s41467-018-03793-w.

[4] X. Jiang, L. Sharma, V. Fung, S.J. Park, C.W. Jones, B.G. Sumpter, J. Baltrusaitis, Z. Wu, Oxidative Dehydrogenation of Propane to Propylene with Soft Oxidants via Heterogeneous Catalysis, ACS Catal. 11 (2021). https://doi.org/10.1021/acscatal.0c03999.

[5] J.F.S. de Oliveira, D.P. Volanti, J.M.C. Bueno, A.P. Ferreira, Effect of CO2 in the oxidative dehydrogenation reaction of propane over Cr/ZrO2 catalysts, Appl. Catal. A Gen. 558 (2018) 55–66. https://doi.org/https://doi.org/10.1016/j.apcata.2018.03.020.

[6] Y. Gambo, S. Adamu, G. Tanimu, I.M. Abdullahi, R.A. Lucky, M.S. Ba-Shammakh, M.M. Hossain, CO2-mediated oxidative dehydrogenation of light alkanes to olefins: Advances and perspectives in catalyst design and process improvement, Appl. Catal. A Gen. 623 (2021). https://doi.org/10.1016/j.apcata.2021.118273.

[7] M.A. Atanga, F. Rezaei, A. Jawad, M. Fitch, A.A. Rownaghi, Oxidative dehydrogenation of propane to propylene with carbon dioxide, Appl. Catal. B Environ. 220 (2018) 429–445. https://doi.org/10.1016/j.apcatb.2017.08.052.

[8] Z. Zhang, D. He, Z. Huang, S. He, J. Lu, Y. Luo, Flowing-Air-Induced Transformation to Promote the Dispersion of the CrO_x Catalyst for Propane Dehydrogenation, ACS Appl. Mater. Interfaces. 13 (2021). https://doi.org/10.1021/acsami.0c22759.

[9] J. Baek, H. Jin Yun, D. Yun, Y. Choi, J. Yi, Preparation of Highly Dispersed Chromium Oxide Catalysts Supported on Mesoporous Silica for the Oxidative Dehydrogenation of Propane Using CO2: Insight into the Nature of Catalytically Active Chromium Sites, ACS Catal. 2 (2012) 1893–1903. https://doi.org/10.1021/cs300198u.

[10] F. Rahmani, M. Haghighi, B. Mohammadkhani, Enhanced dispersion of Cr nanoparticles over nanostructured ZrO2-doped ZSM-5 used in CO2-oxydehydrogenation of ethane, Microporous Mesoporous Mater. 242 (2017) 34–49. https://doi.org/https://doi.org/10.1016/j.micromeso.2017.01.012.

[11] P. Michorczyk, J. Ogonowski, K. Zeńczak, Activity of chromium oxide deposited on different silica supports in the dehydrogenation of propane with CO2 – A comparative study, J. Mol. Catal. A Chem. 349 (2011) 1–12. https://doi.org/https://doi.org/10.1016/j.molcata.2011.08.019.

[12] Z.-P. Hu, Y. Wang, D. Yang, Z.-Y. Yuan, CrOx supported on high-silica HZSM-5 for propane dehydrogenation, J. Energy Chem. 47 (2020). https://doi.org/10.1016/j.jechem.2019.12.010.

[13] H.-M. Wang, Y. Chen, X. Yan, W.-Z. Lang, Y.-J. Guo, Cr doped mesoporous silica spheres for propane dehydrogenation in the presence of CO2: Effect of Cr adding time in sol-gel process, Microporous Mesoporous Mater. 284 (2019). https://doi.org/10.1016/j.micromeso.2019.04.016.

[14] J. Wang, Y.-H. Song, Z.-T. Liu, Z.-W. Liu, Active and selective nature of supported CrOx for the oxidative dehydrogenation of propane with carbon dioxide, Appl. Catal. B Environ. 297 (2021). https://doi.org/10.1016/j.apcatb.2021.120400.

[15] D. He, Y. Zhang, S. Yang, Y. Mei, Y. Luo, Investigation of the Isolated Cr(VI) Species in Cr/MCM-41 Catalysts and its Effect on Catalytic Activity for Dehydrogenation of Propane, ChemCatChem. 10 (2018). https://doi.org/10.1002/cctc.201801598.

[16] Y. Zhang, S. Yang, J. Lu, Y. Mei, D. He, Y. Luo, Effect of a Ce Promoter on Nonoxidative Dehydrogenation of Propane over the Commercial Cr/Al_2O_3 Catalyst, Ind. Eng. Chem. Res. 58 (2019). https://doi.org/10.1021/acs.iecr.9b03870.

[17] Y. Cheng, T. Lei, C. Miao, W. Hua, Y. Yue, Z. Gao, Single-Site CrO x Moieties on Silicalite: Highly Active and Stable for Ethane Dehydrogenation with CO2, Catal. Letters. 148 (2018) 1375–1382. https://doi.org/10.1007/s10562-018-2348-x.

[18] J. Bae, I. A. Samek, P. C. Stair, R. Q. Snurr, Investigation of the Hydrophobic Nature of Metal Oxide Surfaces Created by Atomic Layer Deposition, Langmuir. 35 (2019) 5762–5769. https://doi.org/10.1021/acs.langmuir.9b00577.

[19] M. Reinke, Y. Kuzminykh, P. Hoffmann, Low Temperature Chemical Vapor Deposition Using Atomic Layer Deposition Chemistry, Chem. Mater. 27 (2015) 1604–1611. https://doi.org/10.1021/cm504216p.

[20] A. Taheri Najafabadi, A.A. Khodadadi, M.J. Parnian, Y. Mortazavi, Atomic layer deposited Co/γ-Al2O3 catalyst with enhanced cobalt dispersion and Fischer–Tropsch synthesis activity and selectivity, Appl. Catal. A Gen. 511 (2016) 31–46. https://doi.org/https://doi.org/10.1016/j.apcata.2015.11.027.

[21] W. Tang, X. Lu, F. Liu, S. Du, J. Weng, S. Hoang, S. Wang, C.-Y. Nam, P.-X. Gao, Ceria-based nanoflake arrays integrated on 3D cordierite honeycombs for efficient low-temperature diesel oxidation catalyst, Appl. Catal. B Environ. 245 (2019) 623–634. https://doi.org/https://doi.org/10.1016/j.apcatb.2019.01.028.

[22] H. Liu, Y. Li, M. Xiang, H. Zeng, X. Shao, Single-Layered MoS2 Directly Grown on Rutile TiO2(110) for Enhanced Interfacial Charge Transfer, ACS Nano. 13 (2019) 6083–6089. https://doi.org/10.1021/acsnano.9b02608.

[23] G.-Q. Yang, H. Wang, T. Gong, Y.-H. Song, H. Feng, H.-Q. Ge, H. Ge, Z.-T. Liu, Z.-W. Liu, Understanding the active-site nature of vanadia-based catalysts for oxidative dehydrogenation of ethylbenzene with CO2 via atomic layer deposited VOx on γ-Al2O3, J. Catal. 380 (2019). https://doi.org/10.1016/j.jcat.2019.10.009.

[24] B. J. O'Neill, D. H. K. Jackson, J. Lee, C. Canlas, P. C. Stair, C. L. Marshall, J. W. Elam, T. F. Kuech, J. A. Dumesic, G. W. Huber, Catalyst Design with Atomic Layer Deposition, ACS Catal. 5 (2015) 1804–1825. https://doi.org/10.1021/cs501862h.

[25] C. Binet, M. Daturi, Methanol as an IR probe to study the reduction process in ceria–zirconia mixed compounds, Catal. Today. 70 (2001) 155–167. https://doi.org/https://doi.org/10.1016/S0920-5861(01)00415-1.

[26] H. Kazerooni, J. Towfighi Darian, Y. Mortazavi, A.A. Khadadadi, R. Asadi, Titania-Supported Vanadium Oxide Synthesis by Atomic Layer Deposition and Its Application for Low-Temperature Oxidative Dehydrogenation of Propane, Catal. Letters. 150 (2020). https://doi.org/10.1007/s10562-020-03189-w.

[27] R. Huang, Y. Cheng, Y. Ji, R.J. Gorte, Atomic Layer Deposition for Preparing Isolated Co Sites on SiO2 for Ethane Dehydrogenation Catalysis, Nanomaterials. 10 (2020). https://doi.org/10.3390/nano10020244.

[28] Z. Lu, R. W. Tracy, M. Leigh Abrams, N. L. Nicholls, P. T. Barger, T. Li, P. C. Stair, A. A. Dameron, C. P. Nicholas, C. L. Marshall, Atomic Layer Deposition Overcoating Improves Catalyst Selectivity and Longevity in Propane Dehydrogenation, ACS Catal. 10 (2020) 13957–13967. https://doi.org/10.1021/acscatal.0c03391.

[29] H. Yan, K. He, I.A. Samek, D. Jing, M.G. Nanda, P.C. Stair, J.M. Notestein, Tandem In2O3 -Pt/Al2O3 catalyst for coupling of propane dehydrogenation to selective H2 combustion, Science (80-.). 371 (2021) 1257–1260. https://doi.org/10.1126/science.abd4441.

[30] N.V. Srinath, A. Longo, H. Poelman, R.K. Ramachandran, J.-Y. Feng, J. Dendooven, M.-F. Reyniers, V. V. Galvita, In Situ XAS/SAXS Study of Al_2O_3 -Coated PtGa Catalysts for Propane Dehydrogenation, ACS Catal. 11 (2021). https://doi.org/10.1021/acscatal.1c03146.

[31] H. Feng, J.W. Elam, J.A. Libera, M.J. Pellin, P.C. Stair, Oxidative dehydrogenation of cyclohexane over alumina-supported vanadium oxide nanoliths, J. Catal. 269 (2010). https://doi.org/10.1016/j.jcat.2009.11.026.

[32] A.-P. Honkanen, S. Ollikkala, T. Ahopelto, A.-J. Kallio, M. Blomberg, S. Huotari, Johann-type laboratory-scale x-ray absorption spectrometer with versatile detection modes, Rev. Sci. Instrum. 90 (2019) 033107. https://doi.org/10.1063/1.5084049.

[33] M. Rovezzi, C. Lapras, A. Manceau, P. Glatzel, R. Verbeni, High energy-resolution x-ray spectroscopy at ultra-high dilution with spherically bent crystal analyzers of 0.5 m radius, Rev. Sci. Instrum. 88 (2017) 013108. https://doi.org/10.1063/1.4974100.

[34] P. Michorczyk, P. Pietrzyk, J. Ogonowski, Preparation and characterization of SBA-1–supported chromium oxide catalysts for CO2 assisted dehydrogenation of propane, Microporous Mesoporous Mater. 161 (2012) 56–66. https://doi.org/https://doi.org/10.1016/j.micromeso.2012.05.011.

[35] A. Rautiainen, M. Lindblad, L.B. Backman, R.L. Puurunen, Preparation of silica-supported cobalt catalysts through chemisorption of cobalt(ii) and cobalt(iii) acetylacetonate, Phys. Chem. Chem. Phys. 4 (2002) 2466–2472. https://doi.org/10.1039/B201168A.

[36] H. Zhu, S. McDonnell, X. Qin, A. Azcatl, L. Cheng, R. Addou, J. Kim, P. D. Ye, R. M. Wallace, Al2O3 on Black Phosphorus by Atomic Layer Deposition: An in Situ Interface Study, ACS Appl. Mater. & Interfaces. 7 (2015) 13038–13043. https://doi.org/10.1021/acsami.5b03192.

[37] S. S. Lee, J. Y. Baik, K.-S. An, Y. D. Suh, J.-H. Oh, Y. Kim, Reduction of Incubation Period by Employing OH-Terminated Si(001) Substrates in the Atomic Layer Deposition of Al2O3, J. Phys. Chem. B. 108 (2004) 15128–15132. https://doi.org/10.1021/jp048038b.

[38] C. E. Nanayakkara, A. Vega, G. Liu, C. L. Dezelah, R. K. Kanjolia, Y. J. Chabal, Role of Initial Precursor Chemisorption on Incubation Delay for Molybdenum Oxide Atomic Layer Deposition, Chem. Mater. 28 (2016) 8591–8597. https://doi.org/10.1021/acs.chemmater.6b03423.

[39] E. V. Skopin, L. Rapenne, H. Roussel, J.-L. Deschanvres, E. Blanquet, G. Ciatto, D.D. Fong, M.-I. Richard, H. Renevier, The initial stages of ZnO atomic layer deposition on atomically flat $In_{0.53}Ga_{0.47}As$ substrates, Nanoscale. 10 (2018) 11585–11596.

https://doi.org/10.1039/C8NR02440E.

[40] J.M. Clary, S.A. Van Norman, H.H. Funke, D. Su, C.B. Musgrave, A.W. Weimer, Highly dispersed Co deposited on Al2O3 particles via CoCp2 + H2 ALD, Nanotechnology. 31 (2020) 175703. https://doi.org/10.1088/1361-6528/ab68e1.

[41] L.T. Zhuravlev, The surface chemistry of amorphous silica. Zhuravlev model, Colloids Surfaces A Physicochem. Eng. Asp. 173 (2000). https://doi.org/10.1016/S0927-7757(00)00556-2.

[42] Z. Hu, C.H. Turner, Initial Surface Reactions of TiO2 Atomic Layer Deposition onto SiO2 Surfaces: Density Functional Theory Calculations, J. Phys. Chem. B. 110 (2006). https://doi.org/10.1021/jp060367b.

[43] A. Mameli, M.J.M. Merkx, B. Karasulu, F. Roozeboom, W. (Erwin) M.M. Kessels, A.J.M. Mackus, Area-Selective Atomic Layer Deposition of SiO_2 Using Acetylacetone as a Chemoselective Inhibitor in an ABC-Type Cycle, ACS Nano. 11 (2017) 9303–9311. https://doi.org/10.1021/acsnano.7b04701.

[44] X. Hu, J. Schuster, S.E. Schulz, T. Gessner, Surface chemistry of copper metal and copper oxide atomic layer deposition from copper(ii) acetylacetonate: a combined first-principles and reactive molecular dynamics study, Phys. Chem. Chem. Phys. 17 (2015) 26892–26902. https://doi.org/10.1039/C5CP03707G.

[45] Q. Ma, F. Zaera, Chemistry of Cu(acac)2 on Ni(110) and Cu(110) surfaces: Implications for atomic layer deposition processes, J. Vac. Sci. Technol. A Vacuum, Surfaces, Film. 31 (2013) 01A112. https://doi.org/10.1116/1.4763358.

[46] A. Mameli, M. A. Verheijen, A. J. M. Mackus, W. M. M. Kessels, F. Roozeboom, Isotropic Atomic Layer Etching of ZnO Using Acetylacetone and O2 Plasma, ACS Appl. Mater. & Interfaces. 10 (2018) 38588–38595. https://doi.org/10.1021/acsami.8b12767.

[47] R.J. Silvennoinen, O.J.T. Jylhä, M. Lindblad, J.P. Sainio, R.L. Puurunen, A.O.I. Krause, Atomic layer deposition of iridium(III) acetylacetonate on alumina, silica–alumina, and silica supports, Appl. Surf. Sci. 253 (2007) 4103–4111. https://doi.org/https://doi.org/10.1016/j.apsusc.2006.09.010.

[48] I.E. Wachs, Infrared spectroscopy of supported metal oxide catalysts, Colloids Surfaces A Physicochem. Eng. Asp. 105 (1995) 143–149. https://doi.org/https://doi.org/10.1016/0927-7757(95)03325-5.

[49] A. Hakuli, A. Kytökivi, Binding of chromium acetylacetonate on a silica support, Phys. Chem. Chem. Phys. 1 (1999) 1607–1613. https://doi.org/10.1039/A808180H.

[50] Q. Yao, Z.-H. Lu, Z. Zhang, X. Chen, Y. Lan, One-pot synthesis of core-shell Cu@SiO2 nanospheres and their catalysis for hydrolytic dehydrogenation of ammonia borane and hydrazine borane, Sci. Rep. 4 (2015) 7597. https://doi.org/10.1038/srep07597.

[51] M.A. Botavina, Y.A. Agafonov, N.A. Gaidai, E. Groppo, V. Cortés Corberán, A.L. Lapidus, G. Martra, Towards efficient catalysts for the oxidative dehydrogenation of propane in the presence of CO2: Cr/SiO2 systems prepared by direct hydrothermal synthesis, Catal. Sci. Technol. 6 (2016) 840–850. https://doi.org/10.1039/C5CY00998G.

[52] P. G. Harrison, W. Daniell, Catalytic Activity, Surface Redox Properties, and Structural Evolution during the Thermal Processing of Chromium-Promoted Ceria Oxidation Catalysts, Chem. Mater. 13 (2001) 1708–1719. https://doi.org/10.1021/cm001193s.

[53] M. Santhosh Kumar, N. Hammer, M. Rønning, A. Holmen, D. Chen, J.C. Walmsley, G. Øye, The nature of active chromium species in Cr-catalysts for dehydrogenation of propane: New insights by a comprehensive spectroscopic study, J. Catal. 261 (2009) 116–128. https://doi.org/https://doi.org/10.1016/j.jcat.2008.11.014.

[54] Y. Cheng, C. Miao, W. Hua, Y. Yue, Z. Gao, Cr/ZSM-5 for ethane dehydrogenation: Enhanced catalytic activity through surface silanol, Appl. Catal. A Gen. 532 (2017) 111–119. https://doi.org/https://doi.org/10.1016/j.apcata.2016.12.025.

[55] S. De Rossi, M. Pia Casaletto, G. Ferraris, A. Cimino, G. Minelli, Chromia/zirconia catalysts with Cr content exceeding the monolayer. A comparison with chromia/alumina and chromia/silica for isobutane dehydrogenation, Appl. Catal. A Gen. 167 (1998) 257–270. https://doi.org/https://doi.org/10.1016/S0926-860X(97)00315-3.

[56] A. Chakrabarti, M. Gierada, J. Handzlik, I.E. Wachs, Operando Molecular Spectroscopy During Ethylene Polymerization by Supported CrOx/SiO2 Catalysts: Active Sites, Reaction Intermediates, and Structure-Activity Relationship, Top. Catal. 59 (2016) 725–739.

[57] C. Moisii, D. Jeffcoat, N. Peek, L. van de Burgt, S.L. Scott, A.E. Stiegman, Do Mono-oxo Sites Exist in Silica-Supported Cr(VI) Materials? Reassessment of the Resonance Raman Spectra, J. Phys. Chem. C. 122 (2018). https://doi.org/10.1021/acs.jpcc.8b03403.

[58] A.J.M. Mackus, M.A. Verheijen, N. Leick, A.A. Bol, W.M.M. Kessels, Influence of Oxygen Exposure on the Nucleation of Platinum Atomic Layer Deposition: Consequences for Film Growth, Nanopatterning, and Nanoparticle Synthesis, Chem. Mater. 25 (2013) 1905–1911. https://doi.org/10.1021/cm400562u.

[59] R.L. Puurunen, Random Deposition as a Growth Mode in Atomic Layer Deposition, Chem. Vap. Depos. 10 (2004) 159–170. https://doi.org/10.1002/cvde.200306283.

[60] M. Mattinen, J. Hämäläinen, F. Gao, P. Jalkanen, K. Mizohata, J. Räisänen, R.L. Puurunen, M. Ritala, M. Leskelä, Nucleation and Conformality of Iridium and Iridium Oxide Thin Films Grown by Atomic Layer Deposition, Langmuir. 32 (2016) 10559–10569. https://doi.org/10.1021/acs.langmuir.6b03007.

[61] J.R.A. Sietsma, A. Jos van Dillen, P.E. de Jongh, K.P. de Jong, Application of ordered mesoporous materials as model supports to study catalyst preparation by impregnation and drying, in: Stud. Surf. Sci. Catal., 2006: pp. 95–102. https://doi.org/10.1016/S0167-2991(06)80895-5.

[62] P.J. Van Den Brink, A. Scholten, A. Van Wageningen, M.D.A. Lamers, A.J. Van Dillen, J.W. Geus, The Use of Chelating Agents for the Preparation of Iron Oxide Catalysts for the Selective Oxidation of Hydrogen Sulfide, in: 1991: pp. 527–536. https://doi.org/10.1016/S0167-2991(08)64615-7.

[63] B. Dragoi, A. Ungureanu, A. Chirieac, V. Hulea, S. Royer, E. Dumitriu, Enhancing the performance of SBA-15-supported copper catalysts by chromium addition for the chemoselective hydrogenation of trans-cinnamaldehyde, Catal. Sci. Technol. 3 (2013) 2319–2329. https://doi.org/10.1039/C3CY00198A.

[64] P. Hari Krishna Charan, G. Ranga Rao, Investigation of chromium oxide clusters grafted on SBA-15 using Cr-polycation sol, J. Porous Mater. 20 (2013) 81–94. https://doi.org/10.1007/s10934-012-9577-y.

[65] A. Chakrabarti, I.E. Wachs, The Nature of Surface CrOx Sites on SiO2 in Different Environments, Catal. Letters. 145 (2015) 985–994. https://doi.org/10.1007/s10562-014-1394-2.

[66] Z. Xie, Y. Ren, J. Li, Z. Zhao, X. Fan, B. Liu, W. Song, L. Kong, X. Xiao, J. Liu, G. Jiang, Facile in situ synthesis of highly dispersed chromium oxide incorporated into mesoporous ZrO2 for the dehydrogenation of propane with CO2, J. Catal. 372 (2019) 206–216. https://doi.org/https://doi.org/10.1016/j.jcat.2019.02.026.

[67] A.N. Matveyeva, N.A. Zaitseva, P. Mäki-Arvela, A. Aho, A.K. Bachina, S.P. Fedorov, D.Y. Murzin, N.A. Pakhomov, Fluidized-Bed Isobutane Dehydrogenation over Alumina-Supported Ga2O3 and Ga2O3–Cr2O3 Catalysts, Ind. Eng. Chem. Res. 57 (2018). https://doi.org/10.1021/acs.iecr.7b04571.

[68] T. Shishido, K. Shimamura, K. Teramura, T. Tanaka, Role of CO2 in dehydrogenation of propane over Cr-based catalysts, Catal. Today. 185 (2012) 151–156. https://doi.org/10.1016/j.cattod.2011.10.028.

[69] R. Jin, J. Easa, D.T. Tran, C.P. O'Brien, Ru-Promoted CO_2 activation for oxidative dehydrogenation of propane over chromium oxide catalyst, Catal. Sci. Technol. 10 (2020) 1769–1777. https://doi.org/10.1039/C9CY01990A.

[70] A. Burri, M.A. Hasib, Y.-H. Mo, B.M. Reddy, S.-E. Park, An Efficient Cr-TUD-1 Catalyst for Oxidative Dehydrogenation of Propane to Propylene with CO2 as Soft Oxidant, Catal. Letters. 148 (2018) 576–585. https://doi.org/10.1007/s10562-017-2282-3.

[71] P. Michorczyk, J. Ogonowski, P. Kuśtrowski, L. Chmielarz, Chromium oxide supported on MCM-41 as a highly active and selective catalyst for dehydrogenation of propane with CO2, Appl. Catal. A Gen. 349 (2008) 62–69. https://doi.org/https://doi.org/10.1016/j.apcata.2008.07.008.

[72] M.A. Botavina, G. Martra, Y.A. Agafonov, N.A. Gaidai, N.V. Nekrasov, D.V. Trushin, S. Coluccia, A.L. Lapidus, Oxidative dehydrogenation of C3–C4 paraffins in the presence of CO2 over CrOx/SiO2 catalysts, Appl. Catal. A Gen. 347 (2008) 126–132. https://doi.org/10.1016/j.apcata.2008.05.037.

[73] Arthouros Aristotelis Iordanidis, Mathematical Modeling of Catalytic Fixed Bed Reactors, University of Twente, 2002.

[74] I. Ascoop, V. V. Galvita, K. Alexopoulos, M.-F. Reyniers, P. Van Der Voort, V. Bliznuk, G.B. Marin, The role of CO2 in the dehydrogenation of propane over WO –VO /SiO2, J. Catal. 335 (2016). https://doi.org/10.1016/j.jcat.2015.12.015.

[75] M.M. Sullivan, A. Bhan, Effects of oxygen coverage on rates and selectivity of propane-CO2 reactions on molybdenum carbide, J. Catal. 357 (2018) 195–205. https://doi.org/https://doi.org/10.1016/j.jcat.2017.11.004.

[76] M. Sullivan, Evolution in structure and function of transition metal carbides during the catalytic activation of C-O, C-H, and C-C bonds, University of Minnesota , 2017.

[77] J. Liu, Y. Nan, X. Huang, J.Q. Bond, L.L. Tavlarides, Continuous esterification of oleic acid to ethyl oleate under sub/supercritical conditions over γ-Al2O3, Appl. Catal. B Environ. 232 (2018) 155–163. https://doi.org/https://doi.org/10.1016/j.apcatb.2018.03.050.

[78] M.J. Wulfers, R.F. Lobo, Assessment of mass transfer limitations in oligomerization of butene at high pressure on H-beta, Appl. Catal. A Gen. 505 (2015) 394–401. https://doi.org/https://doi.org/10.1016/j.apcata.2015.08.016.

[79] F. Zhang, R. Wu, Y. Yue, W. Yang, S. Gu, C. Miao, W. Hua, Z. Gao, Chromium oxide supported on ZSM-5 as a novel efficient

catalyst for dehydrogenation of propane with CO2, Microporous Mesoporous Mater. 145 (2011) 194–199. https://doi.org/https://doi.org/10.1016/j.micromeso.2011.05.021.

[80] D. Fang, J. Zhao, W. Li, X. Fang, X. Yang, W. Ren, H. Zhang, Investigation of the characteristics and deactivation of catalytic active center of Cr-Al2O3 catalysts for isobutane dehydrogenation, J. Energy Chem. 24 (2015) 101–107. https://doi.org/10.1016/S2095-4956(15)60290-X.

[81] C.H. Collett, J. McGregor, Things go better with coke: the beneficial role of carbonaceous deposits in heterogeneous catalysis, Catal. Sci. Technol. 6 (2016) 363–378. https://doi.org/10.1039/C5CY01236H.

[82] S. Gomez Sanz, L. McMillan, J. McGregor, J.A. Zeitler, N. Al-Yassir, S. Al-Khattaf, L.F. Gladden, The enhancement of the catalytic performance of CrOx/Al2O3 catalysts for ethylbenzene dehydrogenation through tailored coke deposition, Catal. Sci. Technol. 6 (2016) 1120–1133. https://doi.org/10.1039/C5CY01157D.

[83] S. Gomez Sanz, L. McMillan, J. McGregor, J.A. Zeitler, N. Al-Yassir, S. Al-Khattaf, L.F. Gladden, A new perspective on catalytic dehydrogenation of ethylbenzene: the influence of side-reactions on catalytic performance, Catal. Sci. Technol. 5 (2015) 3782–3797. https://doi.org/10.1039/C5CY00457H.

[84] C. Glasson, C. Geantet, M. Lacroix, F. Labruyere, P. Dufresne, Beneficial Effect of Carbon on Hydrotreating Catalysts, J. Catal. 212 (2002) 76–85. https://doi.org/10.1006/jcat.2002.3781.

Supporting Information

Highly dispersed atomic layer deposited CrO_x on SiO_2 catalyst with enhanced yield of propylene for CO_2 –mediated oxidative dehydrogenation of propane

Fatemeh Gashoul Daresibi [a], Abbas Ali Khodadadi *[a], Yadollah Mortazavi [a], Simo Huotari [b], Mikko Ritala [c]

[a] Catalysis and Nanostructured Materials Research Laboratory, School of Chemical Engineering, University of Tehran, P.O. Box: 11155/4563, Tehran, Iran

[b] Department of Physics, University of Helsinki, P.O. Box 64, 00014, Helsinki, Finland

[c] Department of Chemistry, University of Helsinki, P.O. Box 55, 00014, Helsinki, Finland

*Corresponding author: khodadad@ut.ac.ir (A.A. Khodadadi)

S1. Grignard reaction

The OH groups of the silica support was measured with Grignard method [1,2] using the experimental set-up illustrated in **Figure S1**. First, the silica support was crushed and sieved using standard sieves of 125-300 µm openings and then heated in a furnace with a rate of 10 °C.min^{-1} to 300 °C and kept at this temperature for 3 h. Subsequently, 0.5 g of the heat-treated silica was added to 10 ml of dehydrated normal decalin. Then, 2 ml of MeMgI (Sigma-Aldrich, 3M solution in diethylether) Grignard reagent was added to the stirred suspension under a controlled flow of N_2. The outlet gas was collected in a gas bag and after 4 h, when the reaction was finished, the resulting gas mixture was analyzed by a gas chromatography equipped with a flame ionization detector (FID) calibrated for methane. Based on the number of moles of produced methane, the number of surface – OH groups was calculated using Eq. S1 [1]:

$$\equiv Si-OH + MeMgI \rightarrow \equiv Si-OMgI + CH_4 \qquad \text{Eq. S1}$$

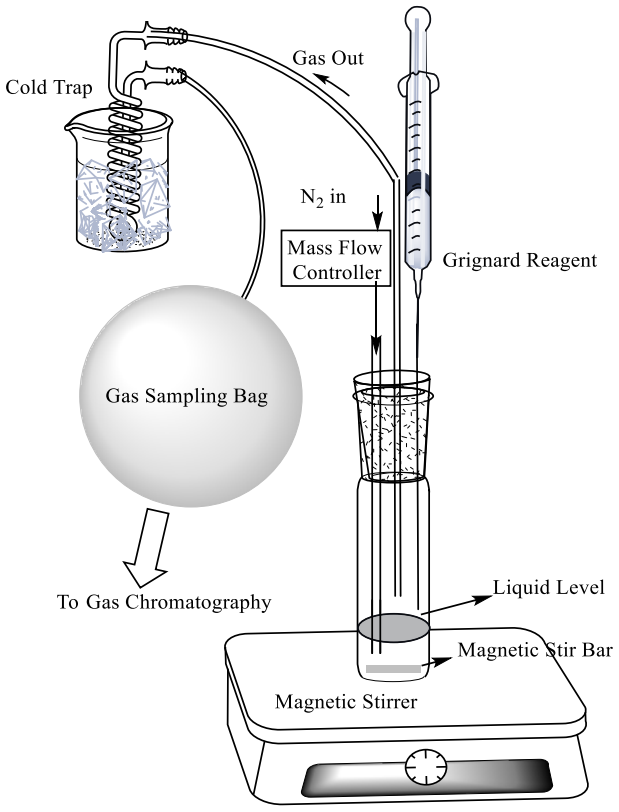

Figure S.1 Schematic diagram of experimental set-up used for Grignard reaction

S2. ALD Setup

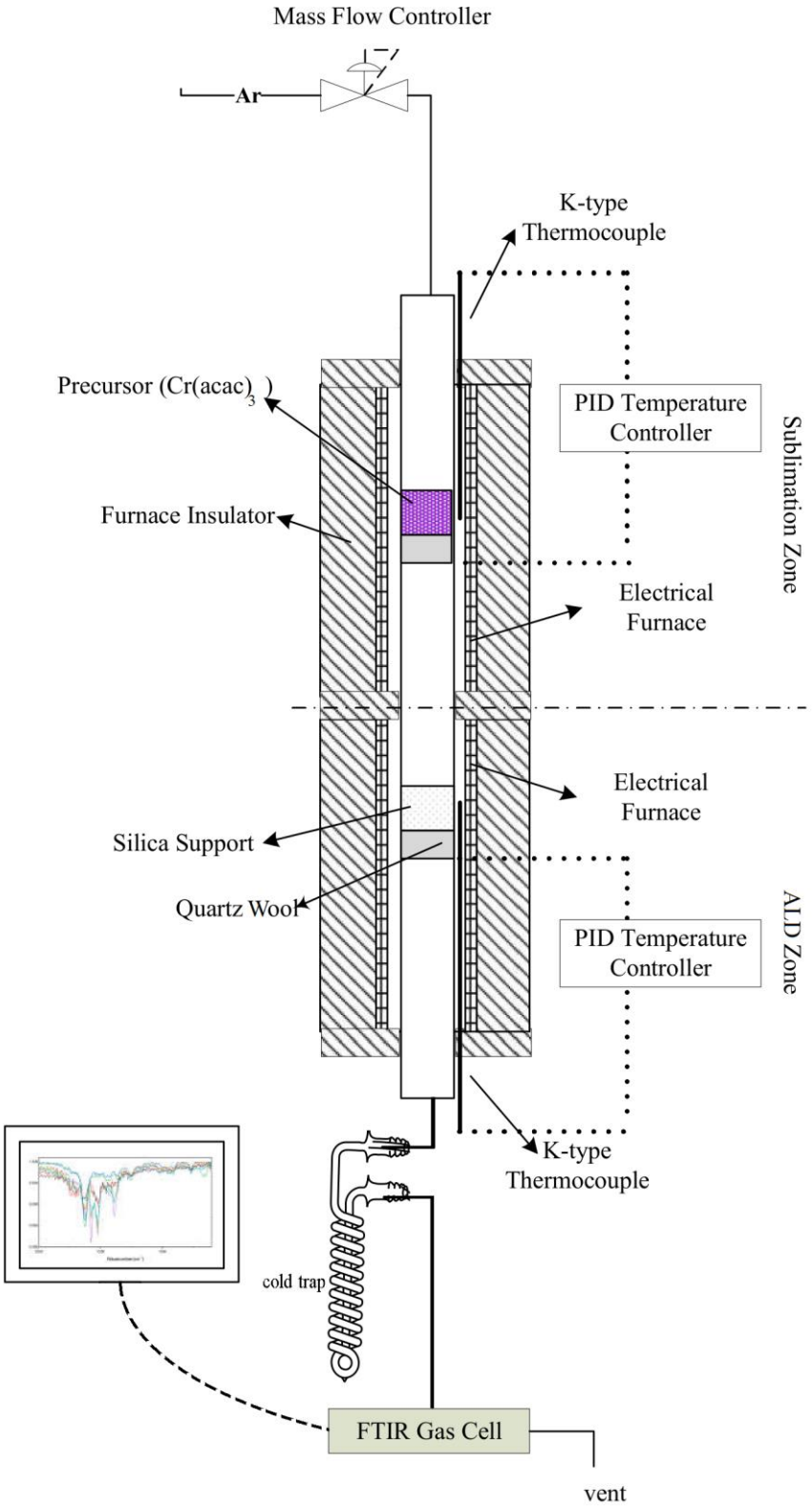

Figure S.2 Schematic diagram of experimental set-up used for the ALD synthesis of catalysts

S3. Laboratory-Scale XANES

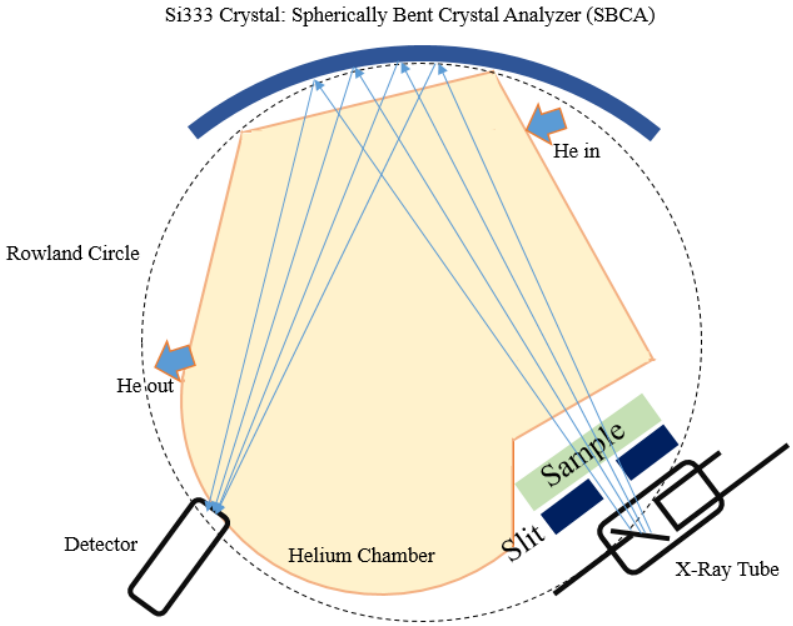

Figure S.3 Schematic diagram of experimental Johann-type Laboratory-Scale set-up used for XANES measurements

S4. Catalytic Performance Test Setup and GC method

S4.1. Test Setup and GC method

Table S. 1 Gas pressures for Varian GC CP 3800 used for the analysis of CO_2-ODHP products

Gas Cylinder	H_2	Ar	Compressed air
Pressure (bar)	4.4	2.5	4

Table S. 2 Gas flowrates for Varian GC CP 3800 used for the analysis of CO_2-ODHP products

	FID compressed air	Ar as Make up gas (FID)	Carrier Gas in packed columns	Carrier gas in capillary column	H_2 Methanizer
Flow ($ml.min^{-1}$)	309.2	21.4	20	5	5.9

Table S. 3 Valve switching time events used in a method in Star Chromatography Workstation for controlling the GC valves during analysis of CO_2-ODHP products

Switching time	Valve 1	Valve 2	Valve 3
Initial	Fill	Forward	Series
0.01	Inject	Forward	Series
0.82	Inject	Forward	Bypass
1.85	Inject	Backflush	Bypass
6.8	Inject	Backflush	Series
8.0	Inject	Backflush	Bypass
17	Fill	Forward	Series

Table S. 4 Time events for controlling oven temperature used in a method in Star Chromatography Workstation for controlling the GC valves during analysis of CO_2-ODHP products

Temperature (ºC)	Rate ($ºC.min^{-1}$)	Hold (min)	Total
80		8	8
190	20	3.5	17

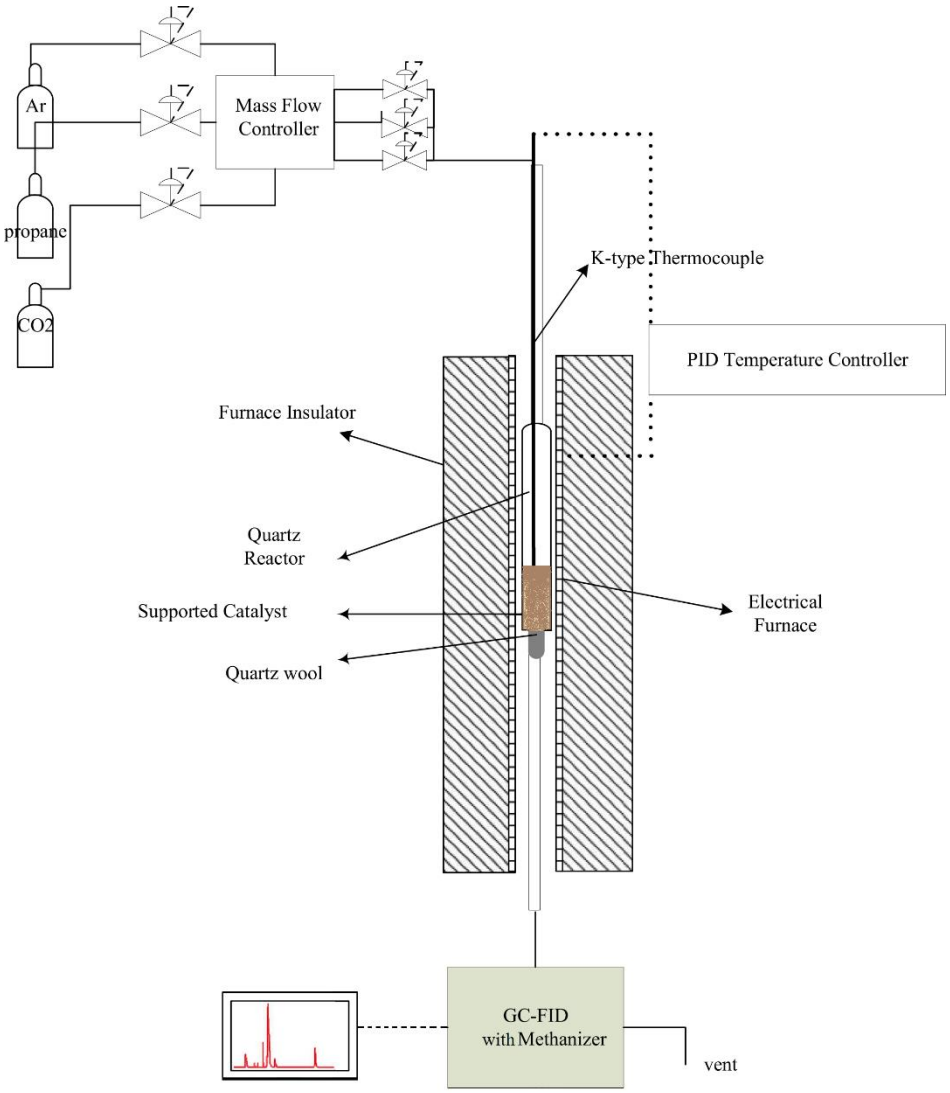

Figure S.4 Schematic diagram of experimental set-up used for CO_2-ODHP reaction

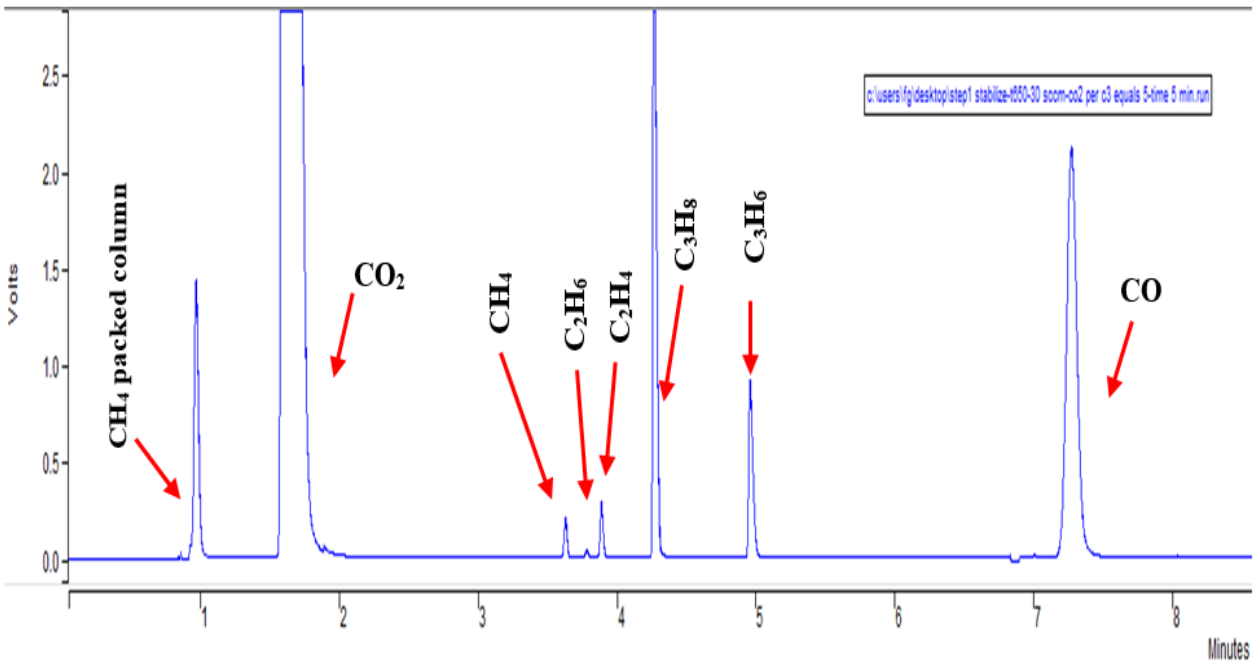

Figure S.5 One of many chromatograms resulted from the analysis of CO_2-ODHP reactor outlet

S4.1. Temperature Programmed Oxidization of Used Catalysts

Standard cylinders of 500 ppm of CO and 1000 ppm of CO_2 in Ar were used to calibrate the evolved gases. The CO and CO_2 formation rate were calculated using Eq. S2. See Le Minh's report [3] for more details.

$$r_{CO\ or\ CO_2}\left[\mu mol.gr_{cat}^{-1}.{}^{\circ}C^{-1}\right]=\frac{50sccm\times\frac{10^6\mu gmol}{22400\ \ Std\ cm^3}\times\left[A_{FTIR\ of\ CO\ or\ CO_2}\times\frac{mol\ fraction_{calibration\ \ gas\ of\ CO\ or\ CO_2}}{A_{FTIR,calibration\ \ gas\ of\ CO\ or\ CO_2}}\right]}{0.050gr_{cat}\times 10{}^{\circ}C/min} \qquad \text{Eq. S2}$$

The coke weight percentage was calculated using Eq. S3:

$$coke\ \ (wt.\%)=12\times10^{-4}\left(\int_{200^{\circ}C}^{700^{\circ}C}(r_{CO}+r_{CO_2})dT\right)\left[\frac{gr_C}{gr_{catalyst}}\right] \qquad \text{Eq. S3}$$

S5. Precursor Properties

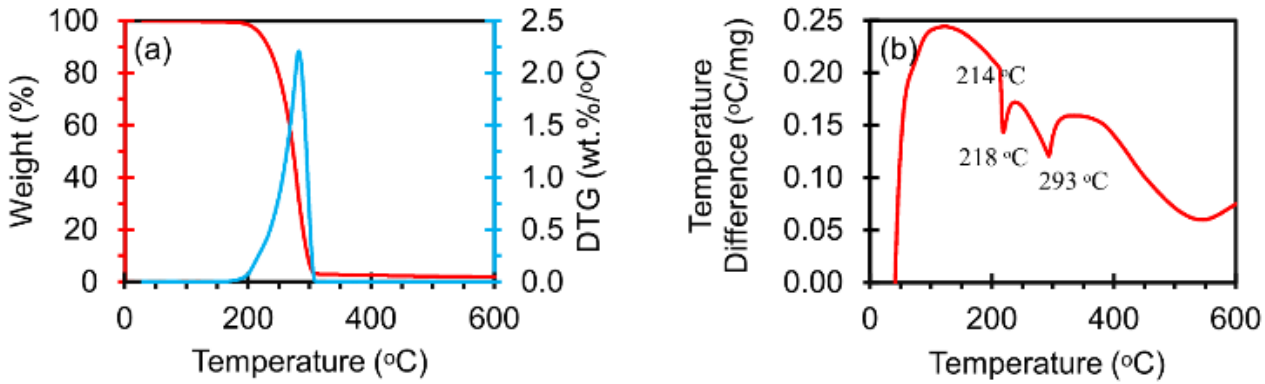

Figure S.6 (a) TGA-DTG and (b) DTA curves of chromium acetylacetonate in N_2 atmosphere at a heating rate of 10 °C.min^{-1}.

S6. ALD Effluent Gas FTIR

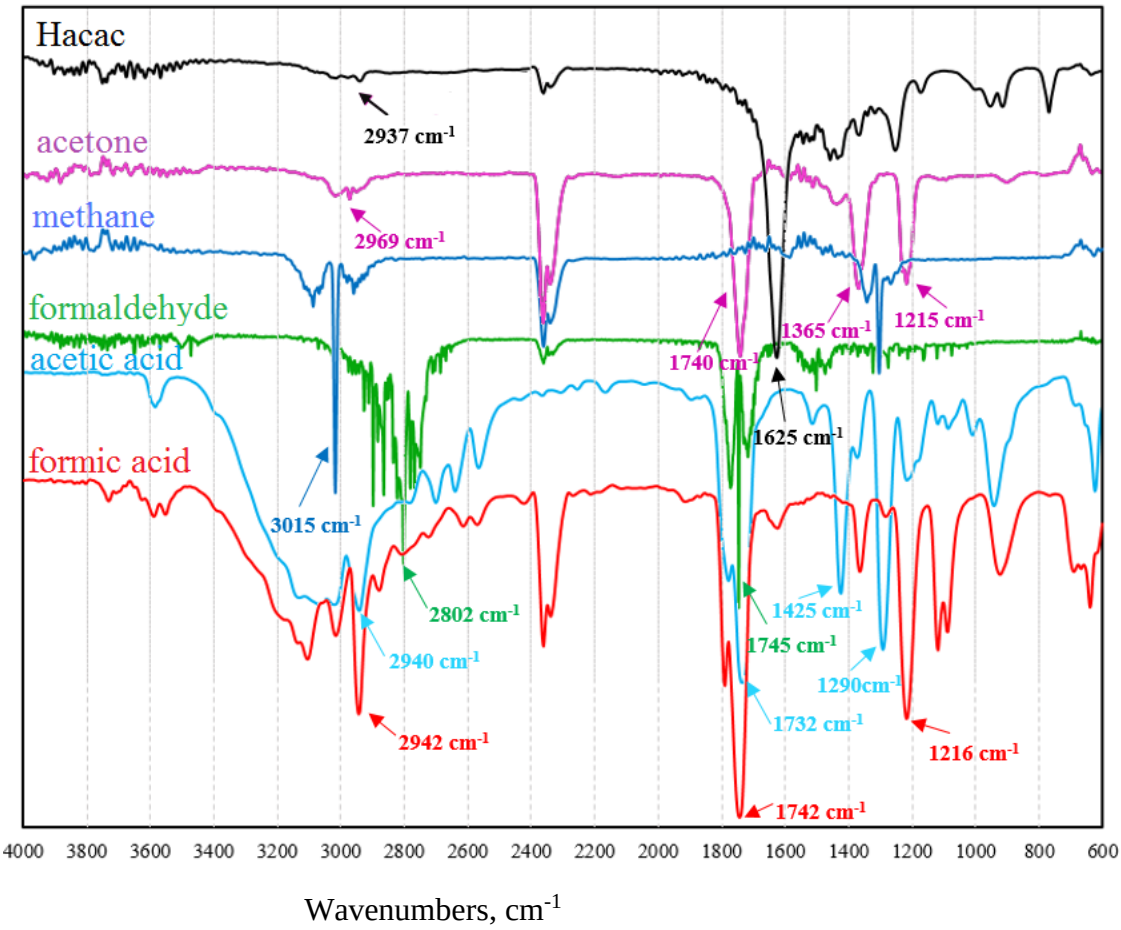

Figure S.7 FTIR spectra of reference gas molecules as possible ALD products for both chemical adsorption and ligand removal steps

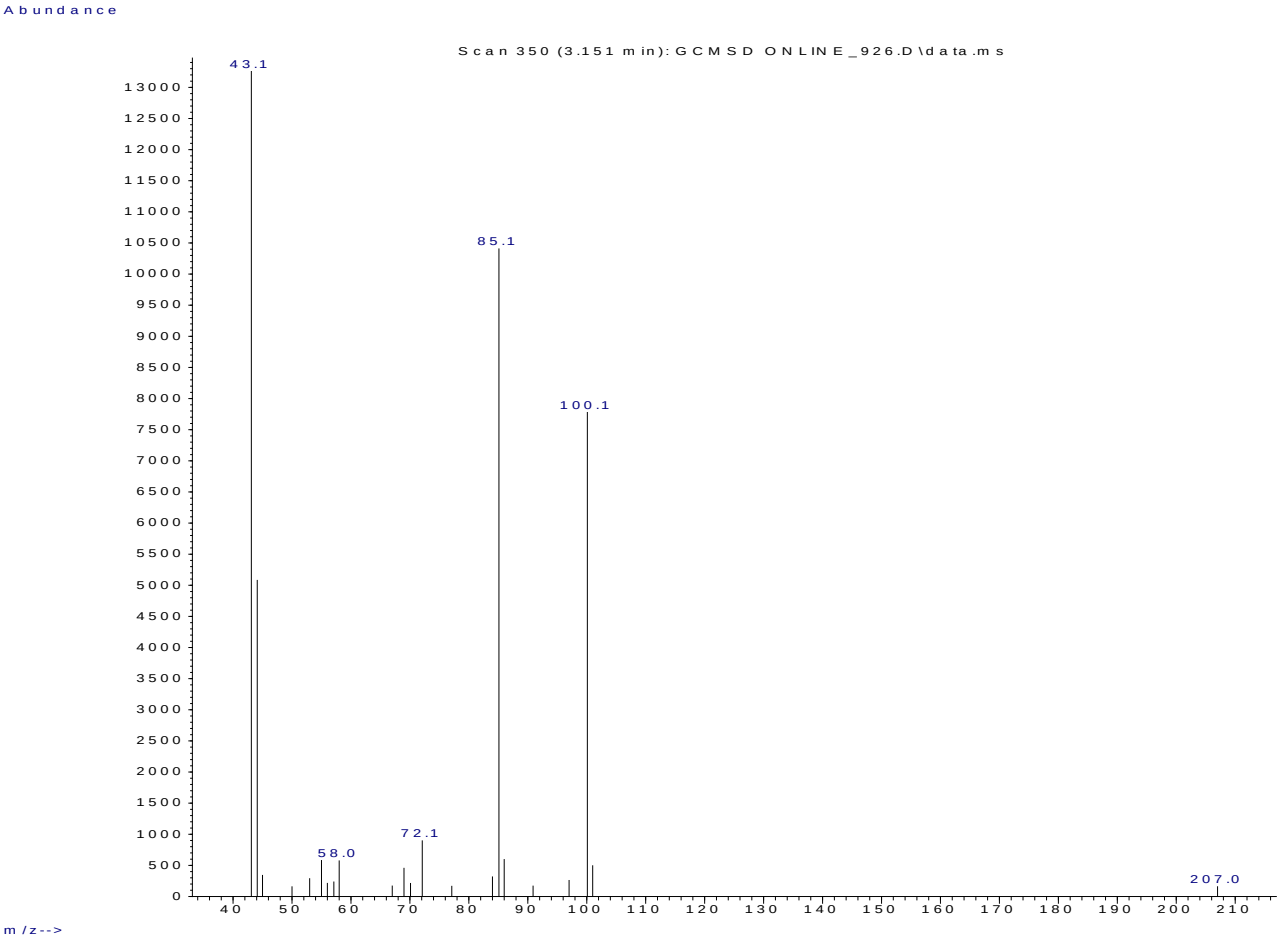

Figure S.8 Mass Spectrum (MS) of outlet gas of ALD reaction on silica at 200 ºC

S7. Characterization of Catalysts

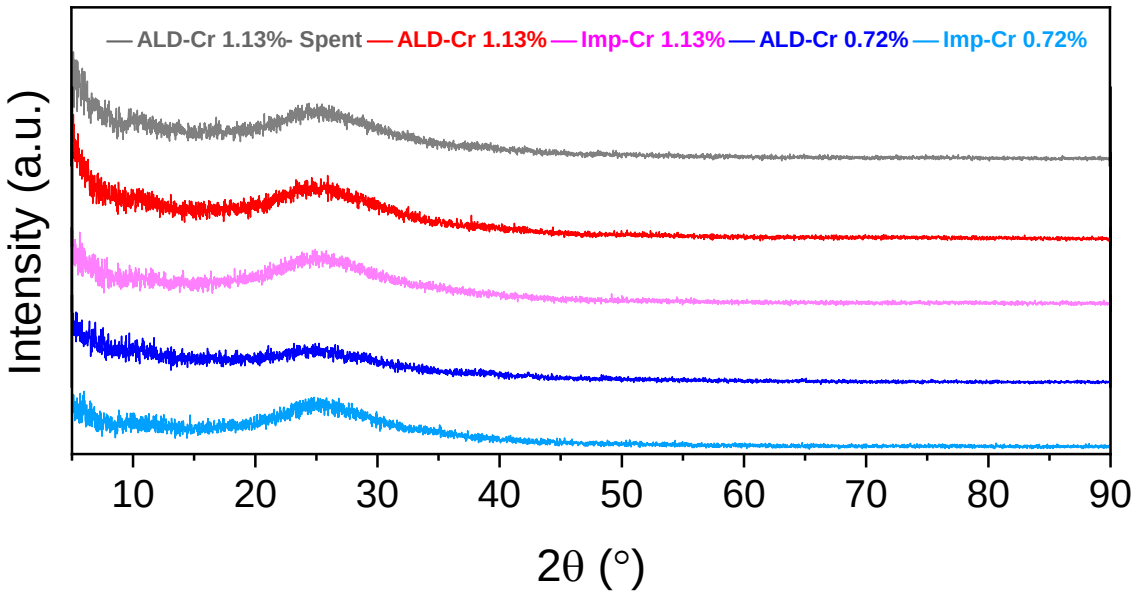

Figure S.9 XRD patterns of the catalysts containing 0.72 and 1.13 wt % Cr by the ALD and impregnation methods and preheated for 1 h at 600 ºC, at which the catalysts were activated before the CO_2-ODHP reaction. The spent ALD-Cr 1.13% was experienced CO_2-ODHP reaction at 600 °C for 8 h TOS.

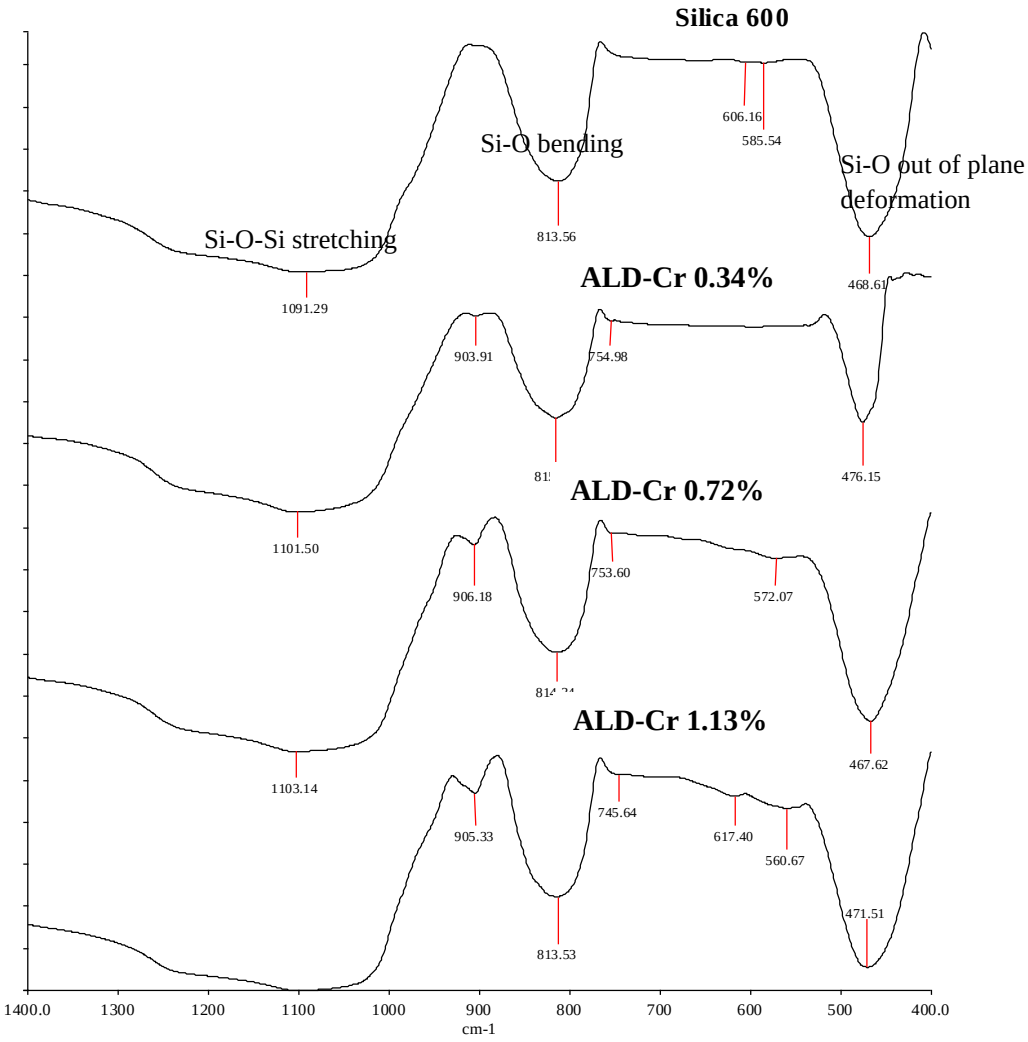

Figure S.10 FTIR spectra of ALD catalyst series and silica support that was calcined similar to other samples. The spectra was normalized and deconvoluted by the software

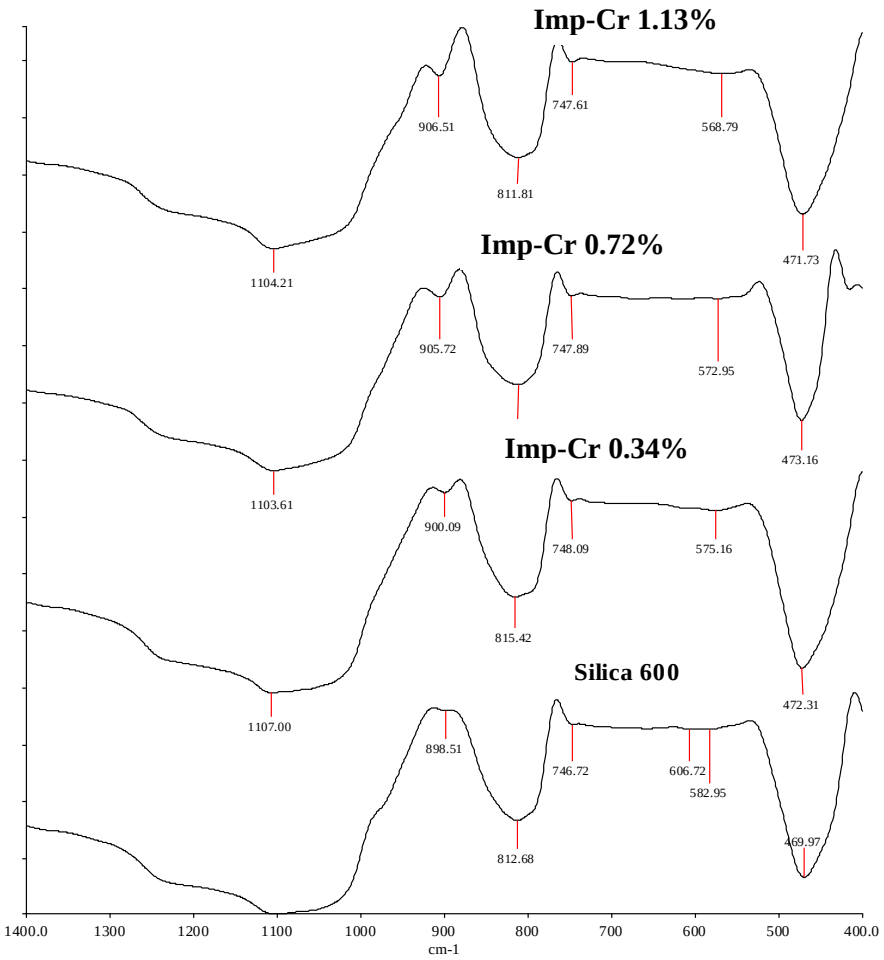

Figure S.11 FTIR spectra of Impregnation catalyst series and silica support that was calcined similar to other samples. The spectra were normalized and deconvoluted by the software

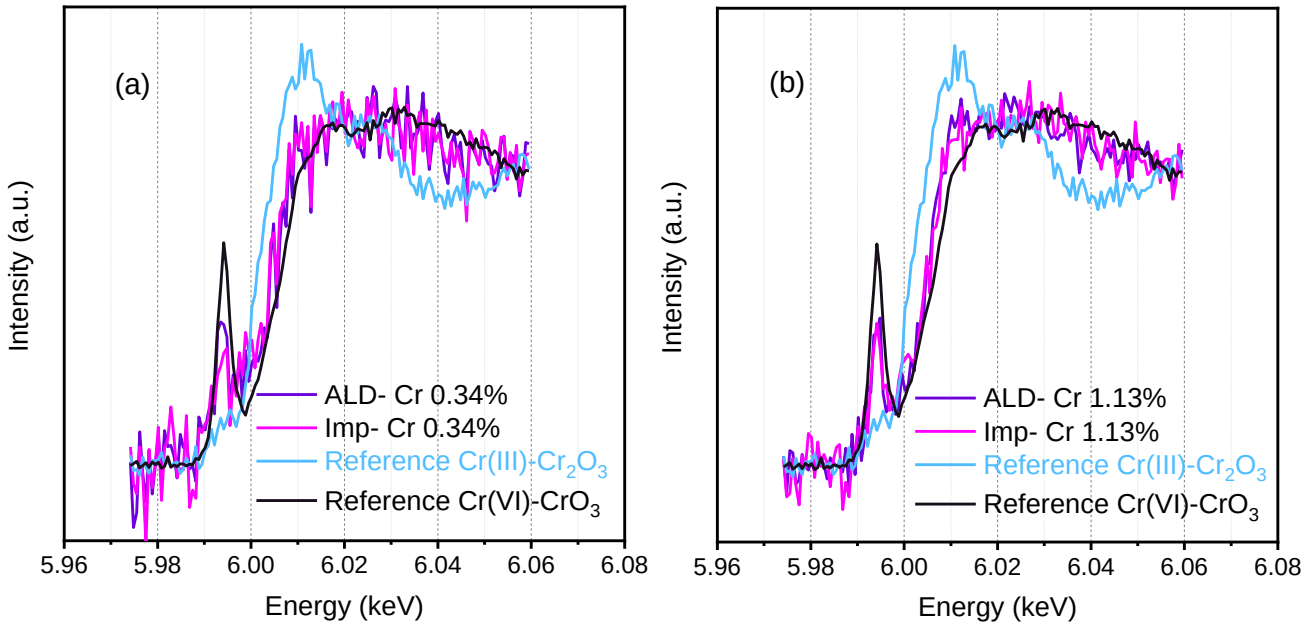

Figure S.12 (a,b) XANES spectra of reference model materials, as-synthesized ALD and impregnation catalysts with a Cr loading of 1.13, 0.34 wt % recorded on Lab-Scale XANES instrument

Table S. 5 UV-Vis peak ranges of silica-based supported chromium oxide catalysts from literatures

Peak range			Assigned to:	Ref.
λ (nm)	1/λ (cm^{-1})*	hv** (eV)		
200-318	~31500-50000	3.9-6.2	$O^{2-} \rightarrow Cr^{6+}$ CT*** of monochromates	[4]
			Cr(VI) in tetrahedral coordination	[5]
			$O^{2-} \rightarrow Cr^{6+}$ CT of chromate species	[6]
			$Cr^{6+}O_x$ ligand to metal charge transfer (LMCT)	[7]
			270nm: $O^{2-} \rightarrow Cr^{6+}$ CT of monochromates	[8]
			270 nm: isolated Cr(VI) oxide in tetrahedral symmetry	[9]
318-424	~24000-31500	2.9-3.9	$O^{2-} \rightarrow Cr^{6+}$ CT of monochromates	[4]
			Cr (VI)	[10]
			Cr(VI) in tetrahedral coordination	[5]
			$O^{2-} \rightarrow Cr^{6+}$ CT of chromate species	[6]
			365nm:$O^{2-} \rightarrow Cr^{6+}$ CT of monochromates	[8]
			$Cr^{6+}O_x$ ligand to metal charge transfer (LMCT)	[7]
			240,348 nm: hydrated dichromate species which shifts to higher λ for hydrated trimmers and tetramers	[11]
			350 nm: isolated Cr(VI) oxide in tetrahedral symmetry	[9]
424-535	~19000-24000	2.3-2.9	Degree of oligomerization	[4]
			Cr (III)	[10]

			$A_{2g} \rightarrow T_{1g}$ of Cr(III) in octahedral symmetry	[5]
			(1) 455 nm: dichromates (2) 465 nm: d-d transition of Cr^{3+} ($A_{2g} \rightarrow T_{1g}$)	[6]
			(1) 460nm: $Cr^{6+}O_x$ ligand to metal charge transfer (LMCT) (2) 425 nm: d-d transition band of Cr^{3+} in pseudo-octahedral	[7]
			429 nm: hydrated dichromate species which shifts to higher λ for hydrated trimmers and tetramers	[11]
			450 nm: The characteristic peak of polychromate Cr(VI) (Cr−O−Cr)n	[8]
			460 nm: polymerized Cr(VI) oxides	[9]
535-700	~14000-19000	1.8-2.3	octahedral symmetry transition of tiny crystalline chromium oxides	[4]
			Cr (III)	[10]
			$A_{2g} \rightarrow T_{2g}$ of Cr(III) in octahedral symmetry	[5]
			d-d transition of Cr^{3+} ($A_{2g} \rightarrow T_{2g}$) in octahedral symmetry like in Cr_2O_3	[6]
			587 nm: d-d transition band of Cr^{3+} in pseudo-octahedral	[11]
			Around 600 nm: octahedral Cr(III) classified as crystalline Cr_2O_3	[8]
			Around 600 nm: crystalline Cr_2O_3	[9]
700-1000	~10000-14000	1.2-1.8	Cr^{5+} Square pyramidal or distorted tetrahedral	[7]

* $\frac{1}{\lambda}(cm^{-1}) = \frac{10^7}{\lambda(nm)}$

** $h\vartheta(eV) = \frac{1240.8}{\lambda(nm)}$

*** Charge Transfer Transition

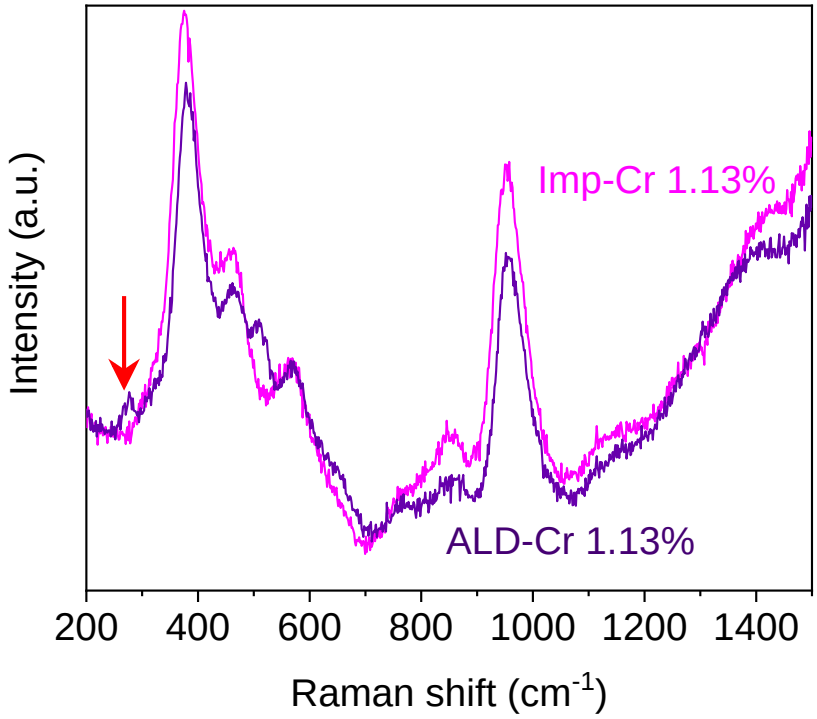

Figure S.13 Raman spectra of ALD and impregnated catalyst with Cr loading of 1.13 wt %

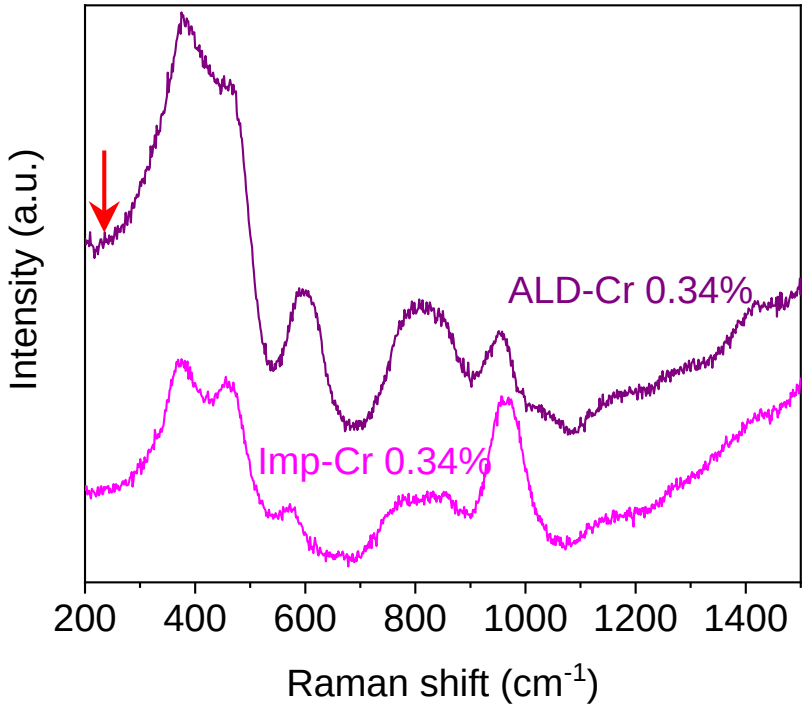

Figure S.14 Raman spectra of ALD and impregnated catalyst with Cr loading of 0.34 wt %

S8. Catalytic Activity:

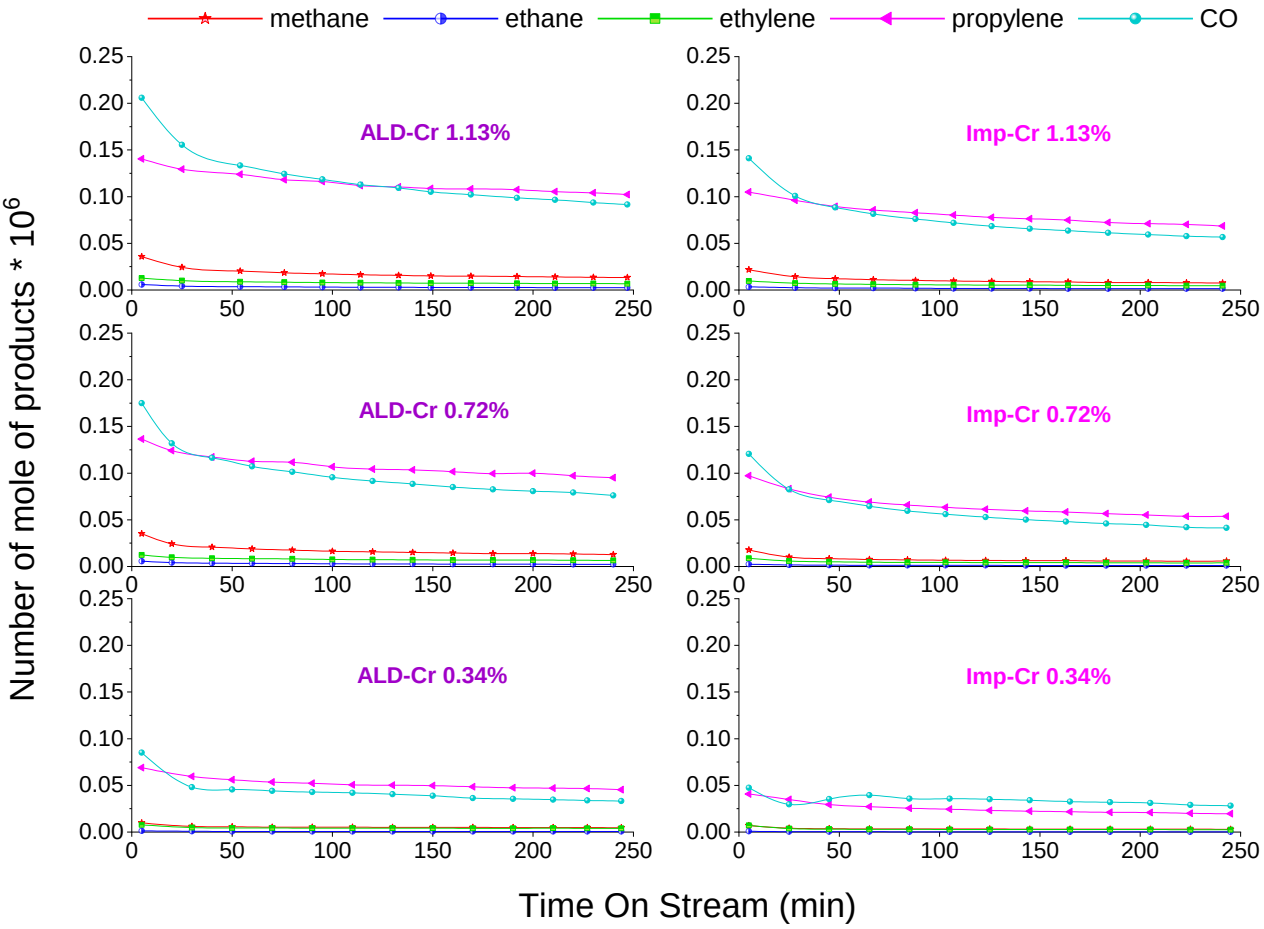

Figure S.15 Number of mole of reaction products as a function of time on steam for all ALD and impregnation catalysts. Reaction condition: T = 600 °C, Total flow rate = 30 sccm, C_3H_8 = 1.5 sccm, CO_2:C_3H_8 = 5:1.

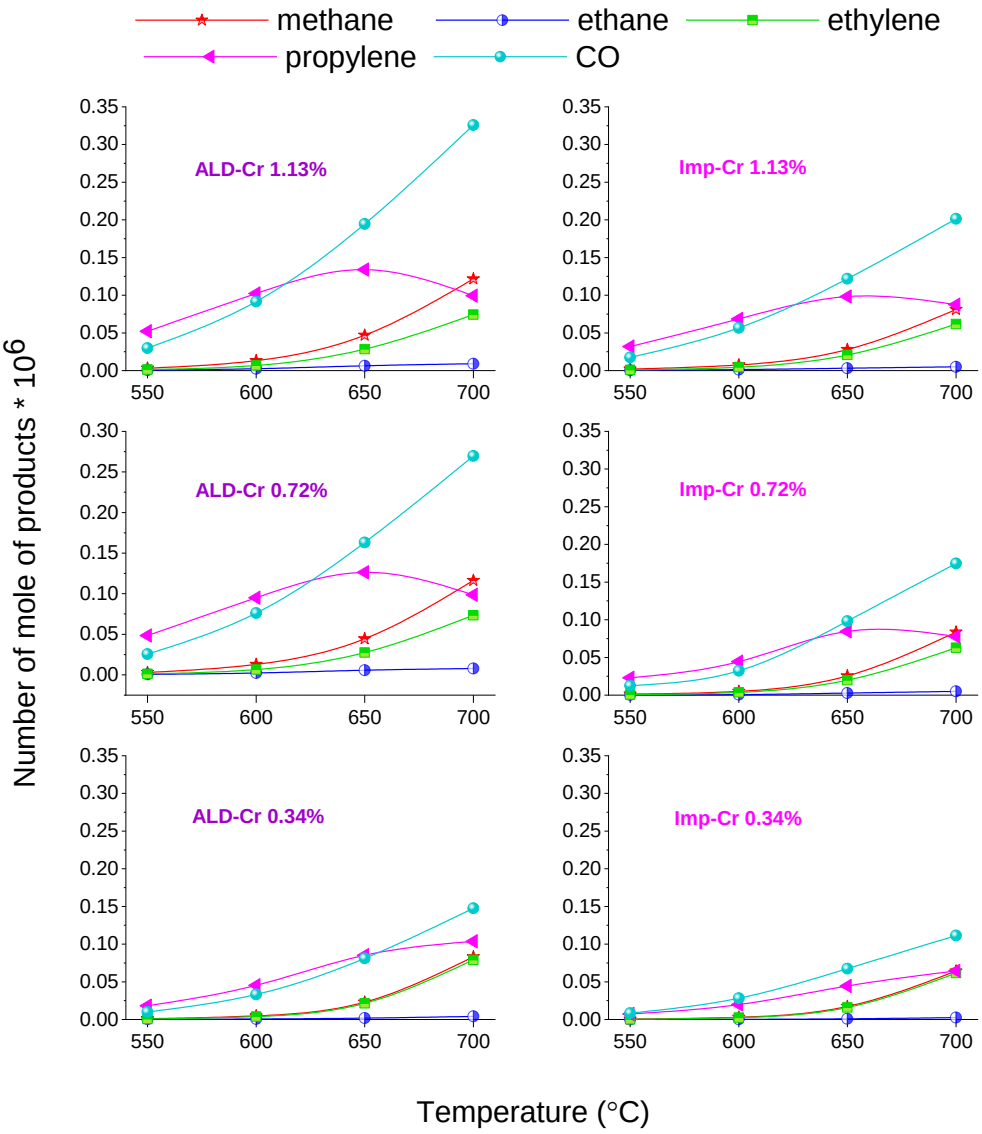

Figure S.16 Number of mole of reaction products as a function of temperature for all ALD and impregnation catalysts. Reaction condition: Total flow rate = 30 sccm, C_3H_8 = 1.5 sccm, CO_2:C_3H_8 = 5:1.

S9. The Investigation of Intrinsic Kinetic Regime with Negligible Mass- and Heat-Transfer Limitations:

To investigate the mass or heat transfer limitations we have used Mears criteria for external heat and mass limitations, Weisz-Prater criterion for internal mass limitation and Biot number for the internal heat limitation [12–14].

For the external mass transfer, we have used the Mears criterion (Eq. S4):

$$\frac{r_{obs}\left(\frac{kgmol}{kgcat.s}\right)\rho_b\left(\frac{kg}{m^3}\right)R(m)n}{k_c\left(\frac{m}{s}\right)C_b\left(\frac{kgmol}{m^3}\right)}<0.15 \qquad \text{Eq. S4}$$

Where r_{obs} is the observed reaction rate, ρ_b is the bed density and can be calculated from $\rho_b = (1-\varphi)\rho_c$ where ρ_c is the density of the catalyst that is 700 kg. m^{-3} for silica as the dominant part of our catalysts. R is the catalyst particle radius, n is the reactant reaction order, k_c is the external mass transfer coefficient and C_b is the reactant bulk concentration.

In a similar way, the Mears criterion was used for the study of the external heat transfer limitation (Eq. S5):

$$\frac{|\Delta H_{rxn}|\left(\frac{kJ}{kgmol}\right)r_{obs}\left(\frac{kgmol}{kgcat.s}\right)\rho_b\left(\frac{kg}{m^3}\right)R(m)E_a\left(\frac{kJ}{kgmol}\right)}{h\left(\frac{kW}{m^2.K}\right)R_g\left(\frac{kJ}{kgmol.K}\right)T_0^2\left(K^2\right)}<0.15 \qquad \text{Eq. S5}$$

Where $|\Delta H_{rxn}|$ is the enthalpy of reaction, E_a is the reaction activation energy, h is the external heat transfer coefficient, R_g is the gas constant (8.314 kJ/kgmol.K) and T_0 is the reaction vessel temperature.

The density of gas mixture was calculated based on the ideal gas assumption (Eq. S6):

$$\rho = P/\bar{R}T \qquad \text{Eq. S6}$$

Where $\bar{R} = \frac{R}{M_{mixture}} = \frac{R}{\sum_{i=1}^{3} x_i MW_i}$

Therefore, we have the density as a function of temperature (Eq. S7):

$$\rho(T)=\frac{\frac{660\times1}{760}(atm)}{\frac{0.082\left(\frac{L.atm}{gmol.K}\right)\times\frac{1m^3}{1000\,L}}{(0.05\times44+0.25\times28+0.70\times18)\left(\frac{g}{gmol}\right)\times\frac{kg}{1000g}}\times T(K)}=\frac{0.868\times21.8}{0.082\,T}=\frac{230.761}{T(K)}\ \left(\frac{kg}{m^3}\right)$$ Eq. S7

which equals to 0.237 kg.m^{-3} at 973 K.

The viscosity of gas mixture was calculated using Eq. S8:

$$\mu_{mix}=\sum_{i=1}^{3}\frac{\mu_i x_i\sqrt{MW_i}}{\sum_{i=1}^{3}x_i\sqrt{MW_i}}$$ [15] Eq. S8

where μ_i, x_i, MW_i as the viscosity, mole fraction and molecular weight of each component was presented in Table S. 6.

Table S. 6 Viscosity of gas mixture obtained from the mixing rule

Component	Ar		C_3H_8		CO_2		mixture
MW (g/gmol)	18		44		28		
x_i (mol fr.)	0.7		0.05		0.25		
μ (μPa.s) / T(K)	Data	Fit	Data	Fit	data	Fit	$\sum_{i=1}^{3}\frac{\mu_i x_i\sqrt{MW_i}}{\sum_{i=1}^{3}x_i\sqrt{MW_i}}$
100	8.1	8.97		2.99		5.49	7.54
200	15.9	15.88		5.67	10.1	10.34	13.56
300	22.7	22.19	8.2	8.24	15	14.97	19.13
400	28.6	28.13	10.8	10.75	19.7	19.47	24.41
500	33.9	33.82	13.3	13.21	24	23.87	29.49
600	38.8	39.30	15.6	15.63	28	28.20	34.43
873		**53.55**		**22.09**		**39.72**	**47.34**
923		**56.06**		**23.26**		**41.79**	**49.63**
973		**58.56**		**24.42**		**43.85**	**51.90**

Reynolds number, $Re=\frac{\rho u d}{\mu(1-\varepsilon_{bed})}$, was calculated as represented in Table S. 7.:

Table S. 7 Reynolds number parameters for the feed gas

T(K)	$\rho_{mixture}$ (kg.m^{-3})	μ mix (Pa.s)	d_{bed} (m)	d_p (m)	u_s(m.s^{-1})= $q_0/(\pi d_{bed}^2/4)$	$Re=\frac{\rho u_s d_p}{\mu(1-\varepsilon_{bed})}$

				0.000		
973	0.237	5.19E-05	0.013	3	0.00475	**0.011**

As Re<1, we have the creeping flow over catalyst particles and therefore Nu=Sh=2 where Nu= $\frac{h(2R)}{k_f}$ and k_f is the thermal conductivity of the gas mixture. Using Wilke's mixing rule, the k_{mix} was calculated (Eq. S9):

$$k_{mix}=\sum_{i=1}^{3}\frac{x_i k_i}{\sum_{j=1}^{3} x_j \varphi_{ij}} \qquad \text{Eq. S9}$$

where x_i is the mole fraction of ith component and $\varphi_{ij}=\frac{\left(1+\left(\frac{\mu_i}{\mu_j}\right)^{0.5}\left(\frac{MW_j}{MW_i}\right)^{0.25}\right)^2}{\sqrt{8}\left(1+\frac{MW_i}{MW_j}\right)^{0.5}}$ [16] which represented in **Table S. 8.**

Table S. 8 The φ_{ij} values for the calculation of thermal conductivity of the gas mixture using Wilke's mixing rule at 700 ºC

φ_{11}	1.00	φ_{21}	0.70	φ_{31}
φ_{12}	1.45	φ_{22}	1.00	φ_{32}
φ_{13}	2.58	φ_{23}	1.73	φ_{33}

Using the viscosities of each component at 973 K, thermal conductivity of gas phase was calculated and reported in

Table S. ***9*****.**

Table S. 9 *Thermal conductivity of each components and the gas mixture using Wilke's mixing rule*

T(K)	k Ar	k Ar fit	k propane	k propane, fit	k CO_2, $mW.m^{-1}.K^{-1}$	k CO_2, fit
100	6.2	6.11				
200	12.4	12.25			9.6	9.59
300	17.9	17.69	18	17.96	16.8	16.83
400	22.6	22.35	30.6	30.72	25.1	25.05
500	26.8	26.51	45.5	45.38	33.5	33.53
600	30.6	30.27	61.9	61.94	41.6	41.59
973		**39.27**		**140.47**		**50.07**

Molecular diffusion coefficient, D_m or $D_{propane\text{-}mixture}$, was calculated by using Eq. S10:

$$D_{propane\text{-}mixture}=\frac{1-y_{propane}}{\frac{y_{CO_2}}{D_{propane\text{-}CO_2}}+\frac{y_{Ar}}{D_{propane\text{-}Ar}}}$$ Eq. S10

Where from Wilke-Lee approach [17] we have (Eq. S11):

$$D_{AB}=\frac{10^{-4}\left(1.084-0.249\sqrt{\frac{1}{M_A}+\frac{1}{M_B}}\right)T^{\frac{3}{2}}\sqrt{\frac{1}{M_A}+\frac{1}{M_B}}}{P_t(r_{AB})^2 f(\frac{kT}{\varepsilon_{AB}})}$$ Eq. S11

To have the D_{AB} value, $f(kT/\varepsilon_{AB})$ and its related parameters were calculated and reported in **Table S.** 10

Table S. 10 Required parameters for the calculation of $f(kT/\varepsilon_{AB})$ in D_{AB}

	r(nm)	ε_i/k	A-B	$r_{AB}(nm)=\frac{(r_A+r_B)}{2}$	$\varepsilon_{AB}/k=\frac{\sqrt{\varepsilon_A\varepsilon_B}}{k}$	(kT/ε_{AB}) at T=973K	$f(kT/\varepsilon_{AB})$ at T=973K
Propane	0.5118	237.1	Propane-CO_2	0.4530	215.13	4.52	0.415
CO_2	0.3941	195.2	Propane-Ar	0.3499	158.28	6.15	0.397
Ar	0.188	105.6[a]					

[a] by $T_{b,\,Ar}$=87.3 K, then: $\varepsilon_{Ar}/k=1.21T_{b,\,Ar}$

Then the other required parameters for the calculation of D_{AB}, were reported in **Table S. *11*.**

Table S. 11 D_{AB} calculation parameters

	MW(g/gmol)	T(K)	Pt (Pa)	r_{AB} (nm)	kT/ε_{AB}	$f(kT/\varepsilon_{AB})$	$D_{AB}(m^2.s^{-1})$
Propane	44	973	87971.05	0.453	4.52	0.415	1.00E-04
CO_2	28						
Propane	44			0.3499	6.15	0.397	2.02 E-04
Ar	18						

Then as $Nu=\frac{h(2R)}{k_f}=2$, at 973 K, h = 508 $W.m^{-2}.K^{-1}$.

Then k_c was calculated by assuming $Sh=k_c(2R)/D=2$.

For enthalpy of reaction when $A+\frac{b}{a}B\rightarrow\frac{c}{a}C+\frac{d}{a}D$, we have (Eq. S12) [18]:

$$\Delta H_{rxn}(T)=\left[\frac{d}{a}H_D^0(T_R)+\frac{c}{a}H_C^0(T_R)-\frac{b}{a}H_B^0(T_R)-H_A^0(T_R)\right]+\int_{T_R}^{T}\left[\frac{d}{a}C_{P_D}+\frac{c}{a}C_{P_C}-\frac{b}{a}C_{P_B}-C_{P_A}\right]dT=\Delta H_{rxn}^0(T_R)+\int_{T_R}^{T}\Delta C_P dT$$ Eq. S12

Hence, for $C_3H_8 + CO_2 \rightarrow C_3H_6 + CO + H_2O$, we have (Eq. S13):

$$\Delta H_{rxn}(T)=\Delta H^0_{rxn}(298)+\int_{298}^{T}\Delta C_P dT=\Delta H^0_{rxn}(298)+\int_{298}^{T}[C_{P_{C_3H_6}}+C_{P_{CO}}+C_{P_{H_2O}}-C_{P_{C_3H_8}}-C_{P_{CO_2}}]dT \quad \text{Eq. S13}$$

C_{pi} and $\Delta C_{p,rxn}$ can be calculated from **Table S. *12***.

Table S. 12 Requirements of the ΔC_{prxn} calculation

	MW kg/kgmol	C_p, kJ/kg.K	$C_{pi}.MW_i$	
CO_2	28	0.844	23.632	
CO	20	1.02	20.4	
C_3H_8	44	1.67	73.48	
C_3H_6	42	1.5	63	
H_2O	18	1.93	34.74	
		ΔC_{prxn}	21.028	$kJ.kgmol^{-1}.K^{-1}$
			0.021028	$kJ.gmol^{-1}.K^{-1}$

Therefore ΔH_{rxn} as a function of temperature is (Eq. S14):

$$\Delta H_{rxn}(T)=164\frac{kJ}{gmol}+(T(K)-298)\times\left(\frac{0.021kJ}{gmol.K}\right)=157.742+0.021\times T(K) \quad \text{Eq. S14}$$

Then ΔH at 973 K is 178.175 ($kJ.gmol^{-1}$)

Finally, the results reported in **Table S. *13*** shows the absence of external mass and heat transfer limitation at 700 ºC.

Table S. 13 The results of the investigations of external mass and heat limitation criteria at 700 ºC

For ALD sample with Cr loading of 1.13 wt.% (The highest conversion of propane)	Mears' Criterion Mass at 700 ºC	Mears' Criterion Heat at 700 ºC
	0.0001	5.43×10^{-10}

Then, Weisz-Prater criterion (Eq. S15) was used to investigate the presence or absence of internal mass transfer limitations. In this criterion we have:

$$C_{WP}=\eta\phi^2=\frac{r_{obs}\left(\frac{kgmol}{kgcat.s}\right)\rho_c\left(\frac{kg}{m^3}\right)(R(m))^2}{D_e\left(\frac{m^2}{s}\right)C_{As}\left(\frac{kgmol}{m^3}\right)} \quad \text{Eq. S15}$$

Where η is the dimensionless effectiveness factor, ϕ^2 is the dimensionless Thiele modulus, D_e is the effective diffusivity and C_{As} is the reactant surface concentration, which is equal to C_b due to the lack of external mass transfer limitations based on Mears criterion.

For the calculation of D_e, first, the mean free path (λ) of propane was calculated from Eq. S16

$$\lambda = \frac{\mu}{P}\sqrt{\frac{\pi RT}{2M}} = 4.2\ nm \qquad \text{Eq. S16}$$

As r_p, from BJH results, is about 2.65 nm the Knudsen diffusion is dominant. Assuming τ=2-10 and obtaining ε from BJH results which is 0.36 in average, we can calculate D_e as in Eq. S17:

$$D_e = \frac{\varepsilon}{\tau} D_{KA} = \frac{\varepsilon}{\tau} \times 9700\, r_p\,(cm)\sqrt{\frac{T\,(K)}{M_A}} = 2.18 \times 10^{-3} - 4.35 \times 10^{-4} \text{ at T } = 700\ ^{\circ}\text{C} \qquad \text{Eq. S17}$$

At this temperature, for the ALD catalysts with the Cr loading of 1.13wt.%, with the highest propane conversion, and by assuming η=1, we have $\phi^2 = (4.33 - 21.6) \times 10^{-5} \ll 1$. Therefore, the mass transfer limitation was negligible.

Biot number (Bi = h (2R)/$k_{effective}$) was used to investigate the internal heat transfer limitations. As the loading of Cr in all of the samples is below 2 wt.%, the thermal conductivity of particles have been assumed as that of pure support that is 1.3-1.5 $W.m^{-1}.K^{-1}$. Then, as porosity is 0.36 which is less than 0.65, the effective thermal conductivity was calculated for T= 700 ºC using the Eq. S18 [19]:

$$\lambda_{effective} = \frac{1}{4}\left(\lambda_p(3v_p - 1) + \lambda_s(2 - 3v_p) + \left(\left(\lambda_p(3v_p - 1) + \lambda_s(2 - 3v_p)\right)^2 + 8\lambda_s\lambda_p\right)^{\frac{1}{2}}\right) \qquad \text{Eq. S18}$$

Where $\lambda_{effective}$ λ_p, λ_s and v_p are the effective conductivity, conductivity of porosity and solid and the porosity of the catalyst respectively.

Then, as mentioned before, the value of h from Nu was calculated which is 508 $W.m^{-2}.K^{-1}$ at 700 ºC. Therefore, the Bi number at the maximum temperature is number 0.141 and therefore the assumption of uniform temperature inside the particle was proved.

S10. TPR of Regenerated Catalysts

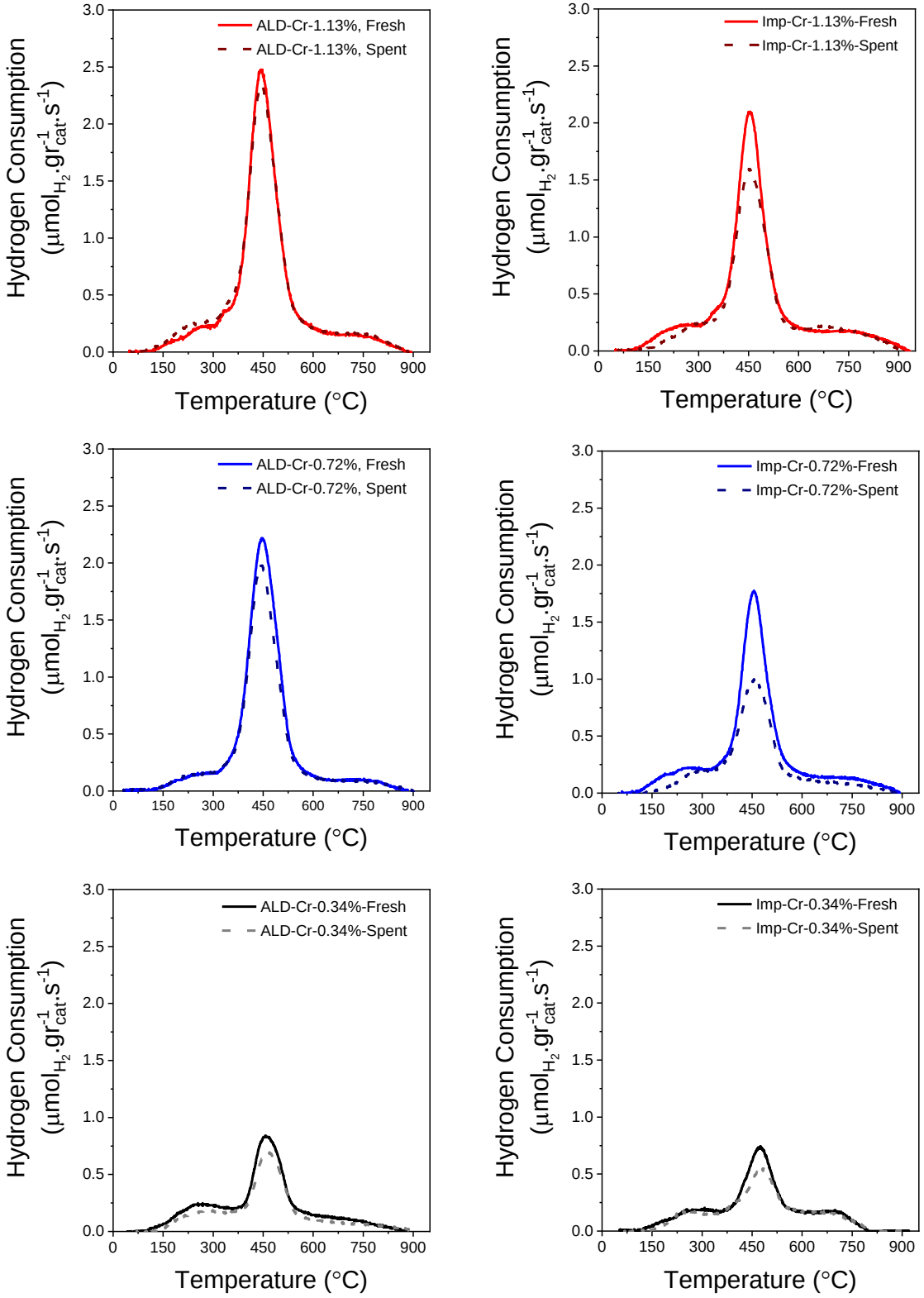

Figure S.17 (a-f) H_2-TPR spectra of as-synthesized and spent ALD and impregnated catalysts. H_2-TPR reaction condition: heating ramp =10 ºC.min^{-1}, 8 sccm 7% H_2 in Ar. The spent catalyst was collected after 6 h time on stream under CO_2-ODHP reaction at 600 ºC with total flow rate of 30 sccm, C_3H_8 = 1.5 sccm, CO_2:C_3H_8 = 5:1 and then regenerated with 4% O_2 in N_2 at 550 ºC for 1 h before TPR experiment.

S11. References of Supporting Information:

[1] J. J. Fripiat, J. Uytterhoeven, HYDROXYL CONTENT IN SILICA GEL “AEROSIL,” J. Phys. Chem. 66 (2002) 800–805. https://doi.org/10.1021/j100811a007.

[2] H. Tamura, A. Tanaka, K. Mita, R. Furuichi, Surface Hydroxyl Site Densities on Metal Oxides as a Measure for the Ion-Exchange Capacity, J. Colloid Interface Sci. 209 (1999) 225–231. https://doi.org/https://doi.org/10.1006/jcis.1998.5877.

[3] C. Le Minh, R.A. Jones, I.E. Craven, T.C. Brown, Temperature-Programmed Oxidation of Coke Deposited on Cracking Catalysts: Combustion Mechanism Dependence, Energy & Fuels. 11 (1997). https://doi.org/10.1021/ef960114p.

[4] Y. Cheng, C. Miao, W. Hua, Y. Yue, Z. Gao, Cr/ZSM-5 for ethane dehydrogenation: Enhanced catalytic activity through surface silanol, Appl. Catal. A Gen. 532 (2017) 111–119. https://doi.org/https://doi.org/10.1016/j.apcata.2016.12.025.

[5] S. De Rossi, M. Pia Casaletto, G. Ferraris, A. Cimino, G. Minelli, Chromia/zirconia catalysts with Cr content exceeding the monolayer. A comparison with chromia/alumina and chromia/silica for isobutane dehydrogenation, Appl. Catal. A Gen. 167 (1998) 257–270. https://doi.org/https://doi.org/10.1016/S0926-860X(97)00315-3.

[6] P. Michorczyk, J. Ogonowski, K. Zeńczak, Activity of chromium oxide deposited on different silica supports in the dehydrogenation of propane with CO2 – A comparative study, J. Mol. Catal. A Chem. 349 (2011) 1–12. https://doi.org/https://doi.org/10.1016/j.molcata.2011.08.019.

[7] A. Chakrabarti, M. Gierada, J. Handzlik, I.E. Wachs, Operando Molecular Spectroscopy During Ethylene Polymerization by Supported CrOx/SiO2 Catalysts: Active Sites, Reaction Intermediates, and Structure-Activity Relationship, Top. Catal. 59 (2016) 725–739.

[8] Z. Zhang, D. He, Z. Huang, S. He, J. Lu, Y. Luo, Flowing-Air-Induced Transformation to Promote the Dispersion of the CrO_x Catalyst for Propane Dehydrogenation, ACS Appl. Mater. Interfaces. 13 (2021). https://doi.org/10.1021/acsami.0c22759.

[9] J. Wang, Y.-H. Song, Z.-T. Liu, Z.-W. Liu, Active and selective nature of supported CrOx for the oxidative dehydrogenation of propane with carbon dioxide, Appl. Catal. B Environ. 297 (2021). https://doi.org/10.1016/j.apcatb.2021.120400.

[10] T.V.M. Rao, E.M. Zahidi, A. Sayari, Ethane dehydrogenation over pore-expanded mesoporous silica-supported chromium oxide: 2. Catalytic properties and nature of active sites, J. Mol. Catal. A Chem. 301 (2009) 159–165.

[11] A. Chakrabarti, I.E. Wachs, The Nature of Surface CrOx Sites on SiO2 in Different Environments, Catal. Letters. 145 (2015) 985–994. https://doi.org/10.1007/s10562-014-1394-2.

[12] M.J. Wulfers, R.F. Lobo, Assessment of mass transfer limitations in oligomerization of butene at high pressure on H-beta, Appl. Catal. A Gen. 505 (2015) 394–401. https://doi.org/https://doi.org/10.1016/j.apcata.2015.08.016.

[13] M. Sullivan, Evolution in structure and function of transition metal carbides during the catalytic activation of C-O, C-H, and C-C bonds, University of Minnesota , 2017.

[14] J. Liu, Y. Nan, X. Huang, J.Q. Bond, L.L. Tavlarides, Continuous esterification of oleic acid to ethyl oleate under sub/supercritical conditions over γ-Al2O3, Appl. Catal. B Environ. 232 (2018) 155–163. https://doi.org/https://doi.org/10.1016/j.apcatb.2018.03.050.

[15] T.A. Davidson, Simple and Accurate Method for Calculating Viscosity of Gaseous Mixtures,

Amarillo, TX, 1993.

[16] B. Todd, J.B. Young, Thermodynamic and transport properties of gases for use in solid oxide fuel cell modelling, J. Power Sources. 110 (2002) 186–200. https://doi.org/https://doi.org/10.1016/S0378-7753(02)00277-X.

[17] R.E. Treybal, Molecular Diffusion In Fluids , in: Mass Transf. Oper., 3rd ed., MC GRAW HILL, 1980: pp. 31–33.

[18] H. Scott Fogler, Essentials for chemical reaction engineering, 2nd ed., Pearson College Div, 2018.

[19] D.S. Smith, A. Alzina, J. Bourret, B. Nait-Ali, F. Pennec, N. Tessier-Doyen, K. Otsu, H. Matsubara, P. Elser, U.T. Gonzenbach, Thermal conductivity of porous materials, J. Mater. Res. 28 (2013). https://doi.org/10.1557/jmr.2013.179.